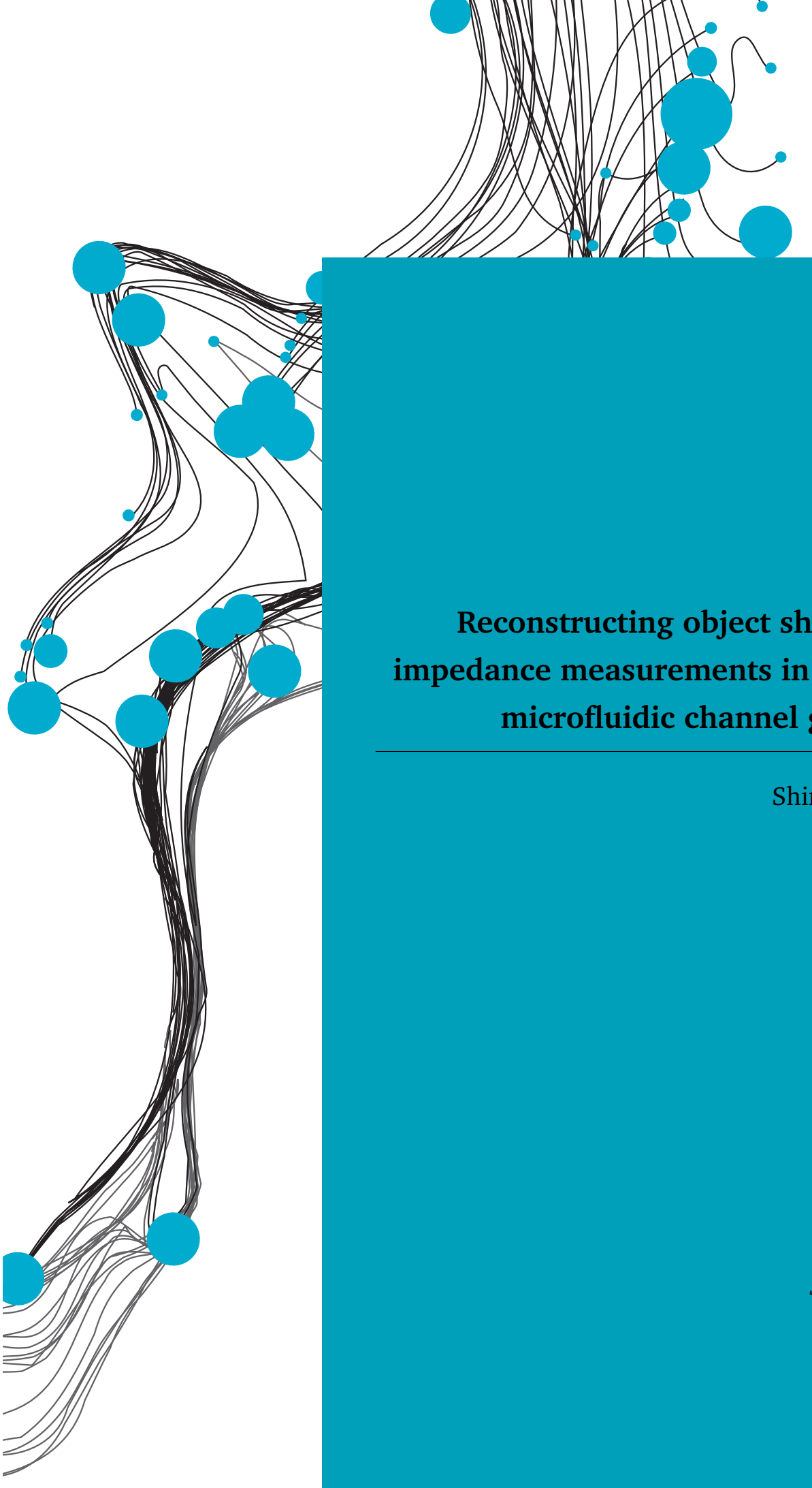

Reconstructing object shape from impedance measurements in a known microfluidic channel geometry

Shing Long Lin

June 24, 2021

UNIVERSITY OF TWENTE.

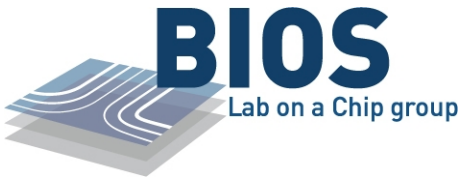

Reconstructing object shape from impedance measurements in a known microfluidic channel geometry

Shing Long Lin

Committee chairman Prof. Wouter Olthuis
BIOS Lab-on-a-chip group, EEMCS
University of Twente

Committee member Prof. Loes Segerink
BIOS Lab-on-a-chip group, EEMCS
University of Twente

External committee member Prof. Raymond Veldhuis
Data management & Biometrics group, EEMCS
University of Twente

Supervisor Stella Kruit, MSc

Article number 2021-1

June 24, 2021

Shing Long Lin

Reconstructing object shape from impedance measurements in a known microfluidic channel geometry

June 24, 2021

Committee: Prof. Wouter Olthuis, Prof. Loes Segerink and Prof. Raymond Veldhuis

Supervisor: Stella Kruit, MSc

University of Twente

BIOS Lab-on-a-chip group

EEMCS deparment

Drienerlolaan 5

7522 NB Enschede

Abstract

In this research a new method is proposed for object shape analysis using impedance measurements of a suspended non-conducting object passing through a microfluidic channel. The method composes a system of resistance equations for discrete object positions as object passes through the channel. This system is then combined with the impedance measurement at each point. The solution of the system of equations is formed by the crosssectional shape of the object. A computational optimizer is used to find the optimal solution to this system that approaches the shape of the object. Shape reconstructions from impedance data generated with COMSOL simulations showed the capability of this method to distinguish shape characteristics typically seen in (abnormal) sperm morphology. However, some artifacts were also present due to simplifications in the resistance model. Experimental measurements of spherical beads lead to shape reconstructions that were within 20% of the object size, but had too many artifacts to say they were of the same shape as the examined object. The experiments have shown the need for further improvement in the setup before practical results can be obtained.

Abstract (Nederlands)

In dit onderzoek wordt een nieuwe methode gepresenteerd voor de analyse van de vorm van een object door middel van impedantie metingen van een niet-geleidend object dat door een microfluidisch kanaal passeert. De methode stelt een systeem van weerstandsvergelijkingen op voor discrete objectposities terwijl het object door het kanaal passeert. Dit systeem wordt vervolgens gecombineerd met de impedantiemetingen van ieder punt. De oplossing van dit systeem van vergelijkingen wordt gevormd door de vorm van de doorsnedes van het object. Een computationele optimaliseerder wordt gebruikt om de optimale oplossing van dit systeem te vinden, die de vorm van het object benadert. Vorm reconstructies van impedantie data gegenereerd met COMSOL simulaties toonden aan dat de methode karakteristieke vormen die worden gevonden in (abnormale) sperma morfologie kon onderscheiden. Echter, waren er vervormingen in de reconstructie aanwezig die werden veroorzaakt door versimpelingen in het weerstandsmodel. Experimentele metingen van ronde microkralen leidden tot vorm reconstructies die binnen 20% van de originele grootte lagen, maar te veel vervormingen hadden om te kunnen zeggen dat ze dezelfde vorm hadden als de kralen. De experimenten lieten zien dat er nog veel verbeteringen nodig zijn in de experimentele opstelling voordat praktische resultaten kunnen worden behaald.

Contents

1 Background

Artificial insemination (AI) is the most used method for reproduction in the veterinary industry. AI allows a single male to fertilize many females, efficiently spreading their beneficial characteristics, without the need for transportation of either sex towards the other. More than 90% of pig and more than 80% of cattle are bred using AI. [1]

For optimal results in AI, it is vital to select the spermatozoa of the highest quality. Characteristics of interest are the sperm vitality, motility and morphology.[2] Normal morphology of spermatozoa is important as it has been correlated with the fertility of the sperm [3]. Figure 1.1 shows an overview of possible malformations in human spermatozoa. Several malformations that occur in spermatozoa can be compensated for by increasing the administered sperm dose. These include small tail abnormalities and proximal or distal cytoplasmic droplets. Malformations of the head, which carries the genetic material, and the mitochondrial sheet, which is vital for the movement of the flagellum, are called primary abnormalities. They are the most severe and cannot be compensated for with larger doses.[1] It is therefore important to identify as many of these morphological abnormalities to provide the best AI success rate.

To assess the characteristics that signal high sperm quality, various tests have been developed like swim up-technique and density gradient centrifguation [4][1] in addition to general methods like flow cytometry and various forms of microscopy. Microscopic examination of spermatozoa can provide most of the required information, but it requires trained personnel, is a tedious process and is subject to bias. Computer aided sperm analysis (CASA) automates this process by performing image analysis using computer programs, which are able to determine most, if not all relevant characteristics for sperm quality, including sperm count, sperm motility and sperm morphology.

Although CASA is able to identify sperm quality, it lacks the ability to sort out the high-quality sperm. This is where microfluidics are able to offer an advantage. Microfluidics is the field that deals with manipulations of fluids on the micrometer scale, which allows for interactions on the single cell level. Various microfluidic analysis methods with filtering and sorting mechanisms are available, among which several have been tested on spermatozoa. [5] [6] [7] Microfluidics offers the advantages of standardization, low cost and scalability and therefore may provide an interesting approach for future sperm analysis.

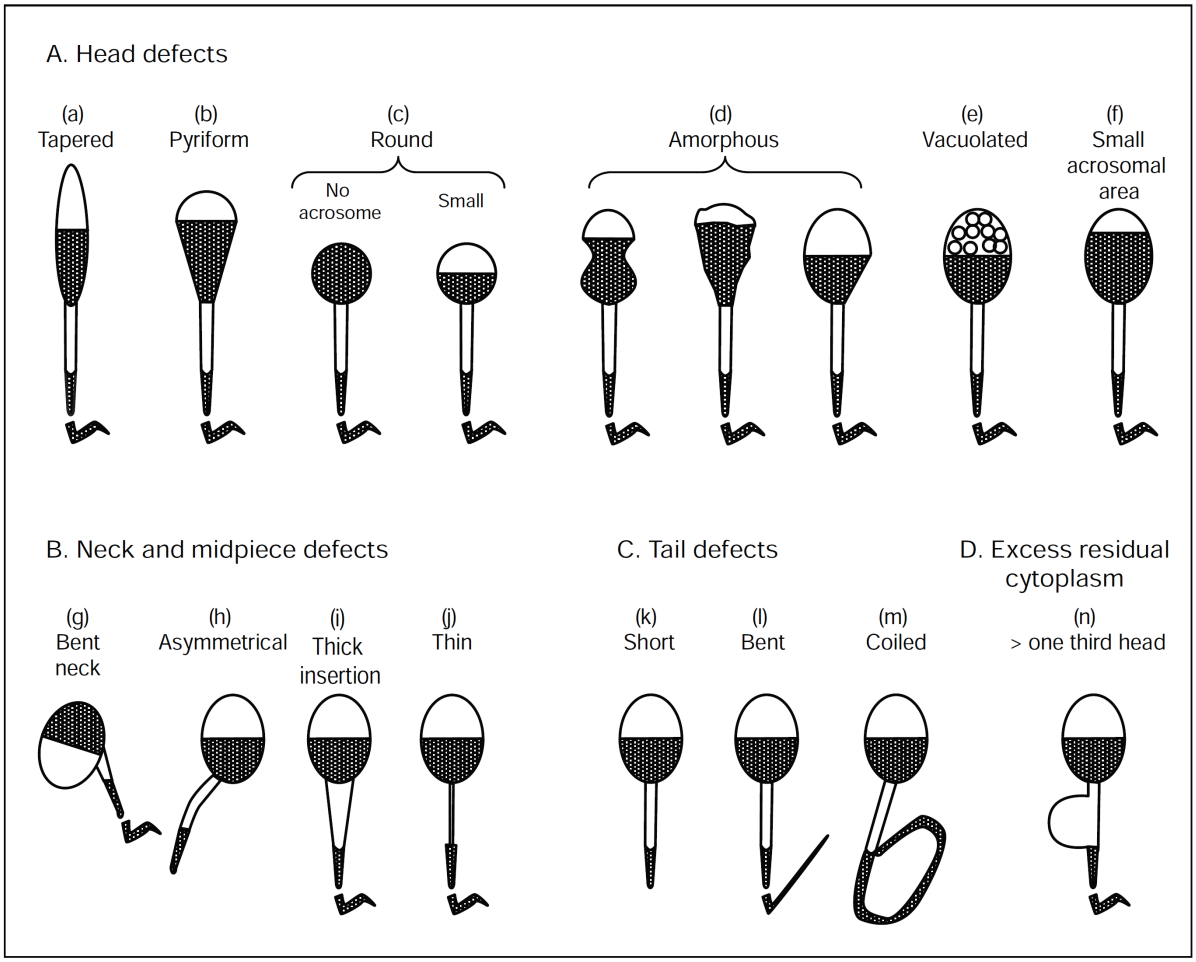

Fig. 1.1.: Overview of possible malformations in human spermatozoa. [3]

Microfluidic analysis of cell morphology may take place using various mechanisms, among which are optical, chemical or electrical sensing methods [8]. Optical methods use light in or outside the visible range to detect and analyse specimen, but require light sources, optics and light sensors, which usually translate to a bulky and expensive setup. Chemical methods can have great selectivity in binding specific molecules or labeling them with e.g. fluorophores, but often require cleaning of substrates or the addition of reactants and may affect the samples, rendering them unfit for further use. Electrical methods, like resistive pulse sensing (RPS), can provide a relatively inexpensive solution that can perform cell morphology analysis without irreversibly affecting the sample.

Two principles have recently been developed in the BIOS research group that might be used for analysis of sperm cell morphology. In appendix E of his doctorate thesis 'Ion Concentration Polarization'[9], Vasilis Papadimitriou proposed a mechanism through which impedance measurements taken of objects in a specifically shaped microfluidic channel could be used to analyse the shape of the object. The movement of the object relative to the shape of the channel

resembled the shifting that functions experience in a mathematical convolution operation and therefore deconvolution might be used to reconstruct the object shape from a resistance profile generated by an object moving through a conducting channel.

The second method is based on the method that Bjorn de Wagenaar presented in his paper 'Towards microfluidic sperm refinement: impedance-based analysis and sorting of sperm cells'[5]. In this paper, cytoplasmic droplets on boar spermatozoa were detected by measuring peaks in the differential impedance signal, while the spermatozoa passed through a set of facing electrodes. By examining the area under the curve for the impedance signal, cytoplasmic droplets could be detected. Following this, the presented platform was also able to sort out the cells with cytoplasmic droplets using dielectrophoresis (DEP).

Cell morphology examination using electrical methods is a relatively unexplored field as optical methods are usually the only methods capable of detecting the subtle morphological differences which are relevant, outside of cell sizing, for which electrical methods are commonly used. The clear morphological differences which abnormally formed sperm cells exhibit however, in combination with the cell-level manipulations that microfluidics offer, provide for an extraordinary opportunity for original research.

2 Introduction

2.1 Research problem

As stated in the background, it is of great relevance to the efficiency and efficacy of artificial insemination to use healthy spermatozoa. Existing methods are able to analyse cell morphology, but are unable to provide sorting of the healthy cells without affecting the sample. Microfluidic devices may provide sorting mechanisms in addition to affordable and scalable analysis methods. Among these methods, electrical measurements provide a cost advantage when compared to optical methods and are label-free, which is an advantage as labels may affect samples and prohibit their further use. The theory that Papadimitrou proposed in his thesis might be used for a novel method of electrical analysis of sperm morphology. With this background, the following research question and sub-questions were proposed:

2.1.1 Research question

How can we identify motility and morphology characteristics of spermatozoa using resistive pulse sensing (RPS)?

Sub-questions

1. Is channel-convolution RPS a viable method of detecting sperm characteristics?
2. Which characteristics are relevant for identification?
3. Which channel design is optimal for revealing the relevant characteristics using channel convolution?
4. Can machine learning aid in the classification of sperm characteristics?

2.2 Research objective

The main objective of this research was to develop a method using electrical impedance measurement that is able to detect defects in boar spermatozoa. As this is a new research that has to be developed from the fundamentals, delivering a proof of concept is the end goal of this research.

For use in future applications, the result of the research should achieve the following objectives:

- Ability to identify morphology characteristics typical of (unhealthy) spermatozoa.
- Relatively simple implementation for shorter development time of the method and lower application cost.
- Possibility for high throughput analysis of samples.

2.3 Research approach

Initially, three methods of using electrical impedance measurements to detect morphological differences in boar spermatozoa were examined during the literature review stage. The first method was the channel convolution method based on the proposal by Vasilis Papadimitriou. The second method was based on the method that Bjorn de Wagenaar presented using differential measurement with facing electrodes. The third method used low aspect ratio micropores as proposed by [10][11]. This last method was mostly deemed a fabrication challenge, which was not favorable due to covid-19 regulations restricting cleanroom access. As the first method was expected to provide the most scientific value by examining an entirely new strategy for microfluidic electrical analysis, it was chosen to expand on this option.

It was quickly discovered that the initially proposed solution of deconvolution was not going to work in our approach and a new solution was developed. This new approach composes a system of equations for the resistance in the channel and then solves this system using computational optimization. This newly developed method was termed Shape Reconstruction from Impedance Measurements (SRIM).

Initially, a theoretical approach was taken for the examination of the method. A mathematical model was built in Matlab, including a method for reconstruction of the shape of the object , using a mathematical optimizer. The results of this model showed promise that the concept might work. To further test its ability to work in a real device, additional physical complexity was introduced by generation of resistance profiles with finite element modeling simulations in

COMSOL. The reconstruction results from these simulations showed enough potential to lead to the fabrication of a microfluidic device. Lab experiments were conducted with this device to validate the functionality of the method on microbeads, custom-made microparticles and sperm cells.

2.4 Outline of this thesis

In the section 'Theory', the general principles of microfluidics and computational optimization are shortly explained, alongside a more in depth look on the impedance of objects in conducting channels. The application of this theory is described in the section 'Methods', which starts with a general explanation of the workflow during the research and then delves further in the details of the method in several sections, including the Matlab model, the use of Comsol simulations and the setup that was used for the experimental validation. The results of each phase in the research are then shown and described in the section 'Results'. Subsequently, these research results are discussed in the section 'Discussion' including recommendations for follow up research. Finally, the scientific contribution of this research and the resolution of the research questions is summarized in the conclusion.

3 Theory

In this section, general principles that were used for this project are explained. We start with an overview of microfluidics including the fabrication of microfluidic devices and the physics that govern fluid flow in microfluidics. The second section describes the different theories for the calculation of impedance in fluidic channels with suspended objects. Next, the different layouts for sensing electrodes in a microfluidic channel are discussed and the chapter is concluded with a primer on computational optimization.

3.1 Microfluidics

Microfluidics is the field that specializes in the manipulation of fluids on the micrometer scale. Combining knowledge of various disciplines like physics, chemistry, biology, electrical engineering, and nanotechnology allows for miniaturization of a multitude of processes that would normally be carried out in a lab, resulting in the alternative name 'lab-on-a-chip'. Due to the small scale of microfluidic processes, experiments only require small amounts of sample and have sensitivities on the single-cell scale. Furthermore, there is room for a large amount of experiments to be run in parallel and therefore the procedure is also more standardized. [12] The following two subsections go into the different possible processes for fabrication of microfluidic devices and the physics behind the special fluid flow behaviour that defines microfluidics.

3.1.1 Fabrication of microfluidic devices

Lab-on-a-chip technologies have been greatly facilitated by making use of cleanroom technology developed for the fabrication of semiconductor devices and microelectronics. One of these techniques is photolithography. Photolithography makes use of photosensitive polymers (photoresist), which change solubility on exposure to UV light. A thin layer of photoresist is applied to a solid underlayer (substrate) and illuminated with UV light. By using a lithography mask, exposure can be limited to certain regions in such a way that only the desired 2D shape is exposed. The exposed region changes solubility so that it can either be washed off after exposure (positive photoresist) or remain on the substrate after washing (negative photoresist), see figure

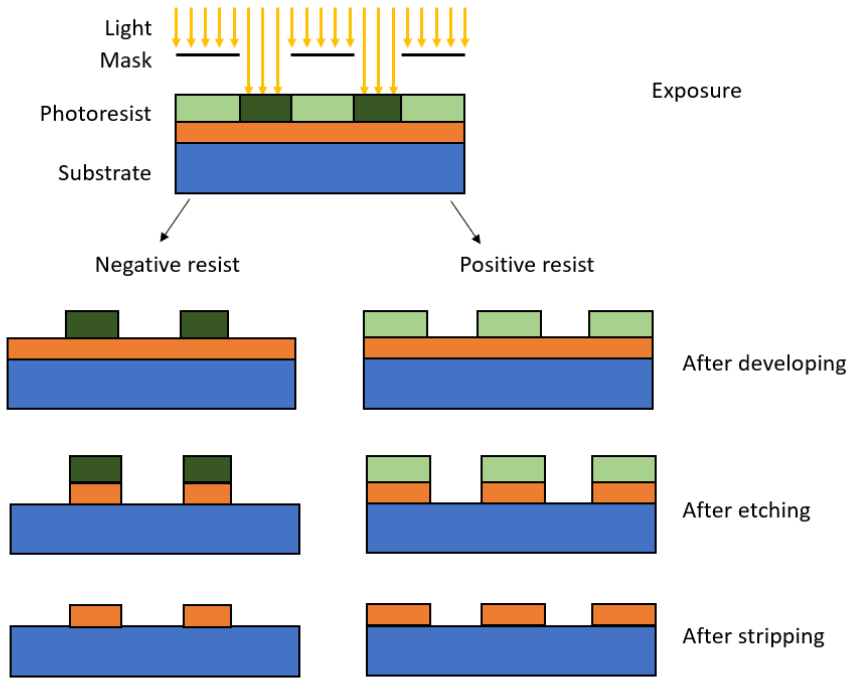

Fig. 3.1.: Illustration of photolithography process with negative and positive photoresist types.

3.1. The photoresist layer can then either be used on its own or serve as a protective layer during etching. Features like channels and chambers can be made in this way. Photolithography techniques allow for precision on the nanometer level.[13]

Soft lithography is a technique that has allowed for cost-effective fabrication of microfluidic chips in the research environment. Although the cleanroom environment and techniques allow for unparalleled precision and freedom of fabrication, usage of the cleanroom is expensive. The solution that soft lithography offers, comes in the form of casting of polymer chips using a positive mold. This mold is fabricated in the clean room, but the subsequent casting of the chips can be done in a relatively low-tech environment. The mold can be reused many (50-100 [14]) times for time and cost efficient production of microfluidic chips. The mold is often made of SU-8, which is a photoresist that is used on its own as a polymeric material, without the typical etching steps of photolithography. SU-8 allows for high aspect ratio features [13] and protocols for processes using SU-8 are well-developed. Polydimethylsiloxane (PDMS) is usually the casted polymer, as its elastomeric properties allow for easy separation from the master, it is optically transparent and it has relatively good biocompatibility. [15]

The final microfluidic chip usually consists of 2 parts. One part contains the spatial features like chambers and channels. The other part is often a flat substrate which acts as a lid for the other part after they are bonded together, forming an airtight enclosure of the features, see figure 3.2.

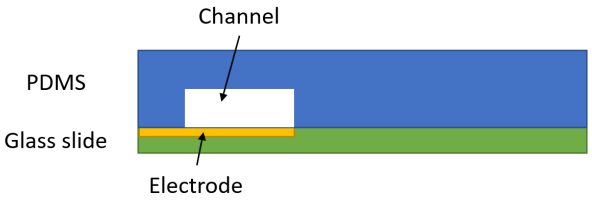

Fig. 3.2.: Typical construction of a PDMS chip containing channels bonded to a glass substrate on which electrodes are sputtered.

In between these two parts might be a spacing layer, which can also contain a second set of channels that for example can be used as valves for actuation. [16]. Bonding can be achieved with several methods, like adhesive bonding with an intermediate glue layer, chemical bonding after plasma activation in the case of PDMS on glass or thermal bonding between two glass layers. [13][17] Plasma activation in PDMS chemical bonding activates the PDMS surface by attachment of reactive silanol (Si-O-H) groups. These can react with nearby silanol groups on the glass surface to form a covalent attachment.

For on chip electrical measurements, electrodes are required. The fabrication of these electrodes generally is done by sputtering a metal layer on the substrate which forms one part of the chip, followed by either lift off technique or etching for removal of deposited metal outside the electrode area. Before bonding of the other part of the chip that contains the channels, these two parts must be aligned so that electrodes are located correctly respective to the channels.

3.1.2 Physics of microfluidic flow

In this section, we continue with the physics behind fluid flow on the microscale.The first distinction that should be made with regards to the flow of fluids is whether this flow takes place in the laminar regime or the turbulent regime. An indicator for this is the Reynolds number, a dimensionless number formed by the ratio of inertial force and viscous force in the fluid, as shown in the following equation with the density ρ, flow velocity v, channel width d and viscosity η: [18]

$$Re = \frac{\text{inertial force}}{\text{viscous force}} = \frac{\rho v d}{\eta} \tag{3.1}$$

Low Reynolds numbers (<10) correspond to laminar flow and high Reynolds numbers (>2000) correspond to turbulent flow. Due to the small dimensions in microfluidic devices and the corresponding low flow velocities, microfluidic devices most often operate in the laminar flow regime. This is characterized by sheet-like flow, where fluid sheets of difference velocities are able to slide by each other without mixing or perpendicular flows.

Laminar flows are fairly predictable due to the lack of chaotic swirling streams. Given a certain external force input, the flow pattern can be determined using the Navier-Stokes equation, simplified here for incompressible flows, P as the externally applied pressure:

$$\rho\frac{dv}{dt} = -\frac{dP}{dy} + \eta\frac{d^2v}{dx^2} \tag{3.2}$$

Pressure driven flow is a common method to transport fluids through microfluidic devices, where a pressure difference is created between the two ends of a channel. Pressure driven flow, also called Poiseuille flow, has a parabolic velocity profile. Due to friction at the walls of the channel, the flow velocity is lowest at the walls. Due to shear forces, the middle of the channel has the highest velocity, with the velocity in the intermediate part decreasing in a quadratic fashion.[19]

The predictable nature of laminar flow can be used for a technique called hydrodynamic flow focusing. By adding two or more side channels that feed into a main channel, the original contents of the main channel can be centered, without mixing of the main and the side streams. Centering of the contents of the main channel can have advantages like reduced clogging of the system and a more uniform flow velocity of the sample. Diffusion however still has to be taken into account for small particles present in the stream, which can easily cover the small distances seen in microfluidic devices and escape the confinement of the middle stream.[20]

3.2 Impedance of objects in fluidic channels

In liquids, electrical currents can travel through the liquid due to migration of dissolved ions. When a potential V is applied across a fluid, the dissolved ions will experience an electric force and due to the induced movement, they will also experience a drag force. These two forces may differ for every ion species. Combined, they form the mobility, μ, of the specific ion species. The mobility of the ions, together with the respective concentrations C of these ions, can be used to calculate the conductivity κ of the solution, see the following equation with the Faraday's constant F and the ion charge magnitude z [21]:

$$\kappa = F\sum_{i=1}^{n}|z_i|\mu_i C_i \tag{3.3}$$

In real life applications, the electrode setup in combination with the conductivity of the measured fluid is going to determine the conductance G that will be measured. The electrode setup and the resulting path that the current will have to take is combined in the system parameter

k, called the cell-constant. The conductance, specific resistance ρ_r, conductivity κ and the cell-constant k relate to each other as follows [21] :

$$\kappa = \frac{1}{\rho_r} = \frac{G}{k} \tag{3.4}$$

For the following paragraphs, it is assumed that the ion concentrations and therefore the conductivity remain constant. Therefore the approximations presented are valid for both conducting solids and liquids, discounting specific boundary effects like the double layer effect. We will revisit these effects at the end of this section.

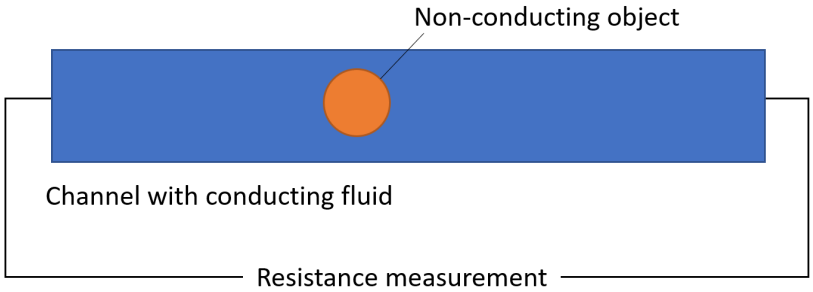

Fig. 3.3.: Non-conducting object in a channel with conductive fluid.

In the next few paragraphs, we look at the effect that non-conducting objects have on the resistance of a channel filled with conductive fluid (illustrated in figure 3.3). To get an exact value for this resistance, Poisson's equation for the potential (equation 3.5), where φ is the potential, ρ_c is the charge density and ε is the permittivity) should be solved with the non-conducting walls of the object and the channel as boundary conditions.

$$\nabla^2\phi = \frac{\rho_c}{\epsilon} \tag{3.5}$$

Solving this equation however is a non-trivial task, especially with atypical object shapes that are not spheres or ellipsoids. Therefore various approximations are used which vary in correctness depending on the relative dimensions of the object to the channel.

Approximation of large particles

If we have a tube of varying cross section, its resistance R can be approximated with its specific resistance ρ_r and the following equation:

$$R = \rho_r \int \frac{dz}{A(z)} \tag{3.6}$$

where A(z) is the cross sectional area perpendicular to the length coordinate z. In case we have a non-conducting object in the tube, *A(z)* will be the cross sectional area of the ring of conducting fluid around the object. J.C. Maxwell had already noted that this approximation gives a lower bound for the resistance as it assumes a homogeneous current density. Any non-uniformity in the current density will lead to an increase in resistance. Therefore, this approximation holds best when the conducting area varies slowly over distance or if the resistance is dominated by the slowly changing part. This second case (shown in figure 3.4) occurs with a large sphere in a tube with almost the same diameter. At the widest part of the object, the influence on the total resistance is highest and the area of the conducting medium changes slowly in the Maxwellian sense. [22]

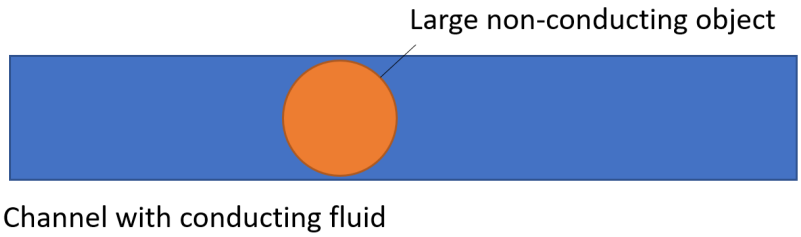

Fig. 3.4.: Channel with a large object relative to the channel dimensions

Approximation of small particles

For a suspension with very small insulating spheres of size d compared to the diameter of the containing channel, D, Maxwell [23] relates the effective conductivity of the mixture (σ_{mix}) to the conductivities of the electrolyte (σ_{el}) and the particles (σ_p):

$$\frac{\sigma_{mix} - \sigma_{el}}{\sigma_{mix} + \sigma_{el}} = f\frac{\sigma_p - \sigma_{el}}{\sigma_p + 2\sigma_{el}} \tag{3.7}$$

Maxwell's equation still holds if the suspension only contains a single sphere. However, this equation only takes into account the far field effects of the electric field and does not include any geometric arrangements. Therefore it is only valid for $d << D$, when the contained sphere is much smaller than the surrounding channel. [24]

When the particles are assumed non-conducting with $\sigma_p = 0$, equation 3.7 can be rewritten using a Taylor's series to:

$$\rho_{eff} = \rho(1 - 3f/2 + ...)$$

Where ρ_{eff} represents the effective resistivity of the dilute suspension of non-conducting spheres in a medium of resistivity ρ, that is based on the volume fraction f of these spheres. Presented by Bean and Deblois[22], this is a recurring form of the equation when it is used for size calculation of suspended objects.

For objects that fall between the limits of the two previously given equations, correction factors for Maxwell's approximation have been proposed that are valid within a certain size regime. Examples of these are the factors proposed by Smythe[25], Gregg and Steidley [26], and Bean and Debois [27], of which the last is still commonly used to relate object size to the measured resistance in resistive pulse sensing, as used in Coulter counters.

Equivalent circuit model

Besides the interactions between the electrolyte and the suspended object, there are additional effects that influence the impedance that is measured. In a microfluidic chip there are for example the resistance of the electrodes and their leads R_Lead, the double layer effect at the electrodes, which can be modelled as a capacitance C_{DL} and parasitic coupling between the electrodes, which causes a capacitance C_{EL}. Furthermore, when measuring with alternating current (AC), dielectric effects have to be taken into account. This means we can no longer measure resistance on its own, but that it is part of the complex impedance, where the capacitive and inductive effects in the circuit also have a contribution.

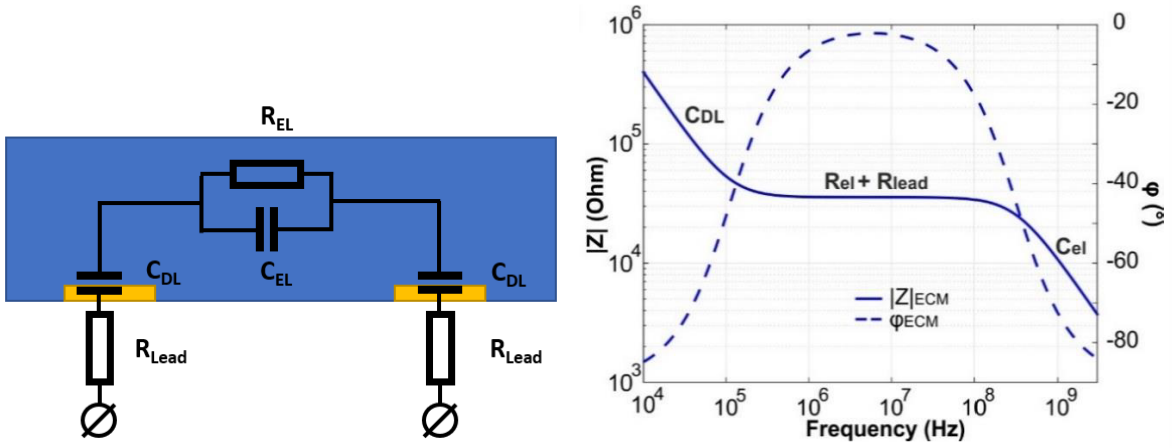

(a) Equivalent circuit model (b) Bode plot

Fig. 3.5.: Electrical characterisation tools for a microfluidic channel: (a) Equivalent circuit model of the SRIM channel without suspended objects (b) Bode plot showing the theoretical impedance and phase frequency response of the SRIM[28]

Each of these effects can be modeled as a linear component in an equivalent circuit model (ECM) [29] [30]. Figure 3.5a shows the equivalent circuit model for the SRIM channel filled

with electrolyte, but without an object. Due to all these different effects, the impedance changes as a function of frequency. At low frequencies, the double layer impedance is the dominant part of the total impedance. At medium frequencies, resistive effects form the dominant part of the total impedance. Then at high frequencies, parasitic capacitative effects dominate the total impedance. The effects of these processes can be seen in figure 3.5b, where a Bode plot, i.e. the system response over a range of frequencies, is shown.

3.3 Electrode configurations for microfluidic impedance measurements

Electrode configurations may vary wildly depending on their purpose, but for cell sensing and impedance measurements, two configurations are commonly used: coplanar electrodes and parallel electrodes. Illustrations of these layouts can be found in figure 3.6.

The coplanar setup consists of two planar electrodes that are positioned near each other in the same plane. For measurements on cells they can be created in the same size range as the cells to provide single cell measurements. Coplanar electrodes were used in the first setup that demonstrated successful differentiation between polymer beads and biological cells. [31] They are simple to fabricate, but create an electric field between the electrodes that is non-uniform in the vertical axis. This non-uniformity can cause variations in measurements depending on the vertical position of the measured cell.

The parallel configuration improves on this design by placing the electrodes on the bottom and the ceiling of the channel. This way, most of the electric field lines run orthogonal to the electrodes and as a result the electric field is homogeneous between the electrodes, apart from the edges where fraying of the field occurs. The precise alignment of the electrodes and the bonding of the substrates increases the complexity of fabrication significantly though. This configuration greatly improves the sensitivity of impedance based measurements on cells

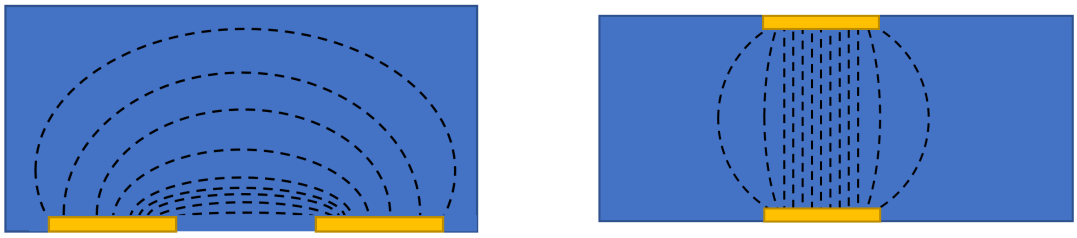

(a) Coplanar

(b) Facing/parallel

Fig. 3.6.: Common electrode configurations for impedance measurements in microfluidic channels.

though, with results showing high enough resolution that cellular features could be detected. [5]

A modification of the coplanar electrodes, presented as 'liquid electrodes' by Shaker et al. aims to combine the positive features of both configurations. It uses coplanar electrodes, spaced apart sufficiently so to allow the electric field to disperse through the full height of the channel. The additional distance required is approximately twice the height of the channel. Although it removes the vertical inhomogeneity of the electric field, it comes at a cost of a lower signal to noise ratio (SNR), as the extra distance will result in additional resistance.[32] [33]

3.4 Computational optimization

The method proposed in this research requires solving of large systems of equations. By making use of computational optimization, the need for a single all-encompassing analytical solution is removed. Furthermore, optimization may provide answers where no exact solutions are possible.

Computational optimization is a field involved with finding the best fitting solution to an often complex problem. Although there are many ways to formulate these problems, generally optimization problems are posed in such a way as to find a minimum or a maximum value to a certain function called the cost function, which is subject to certain constraints. The approach of using computational optimization can be dissected into three distinct parts: the model, the optimizer and the simulator. The model converts a physical problem into mathematical statements. The optimizer describes the method on how to navigate to the optimal solution. The simulator then executes this strategy on the mathematical statements of the model.[34]

There are numerous algorithms available for the optimizer. One of the distinctions that can be made between these algorithms is on whether its optimization strategy requires derivatives of the cost function or whether it is derivative-free. Another characteristic is whether the algorithm is deterministic or that it contains an element of randomness. The latter can be useful for traversing cost functions with local minima.

The algorithm used in this work is based on the Nelder-Mead simplex algorithm, implemented in the Matlab function *fminsearch*. It is deterministic and derivative-free. A simplex is the structure that has n+1 points for the n available dimensions. Examples are a triangle in a 2D space or a tetrahedron in a 3D space. The Nelder-Mead simplex algorithm evaluates the cost function at the corners of the simplex around its current evaluation point. It then replaces the worst performing point with a new point, according to a list of several rules. Depending on the performance of this new point, the simplex can move through reflection, expansion or

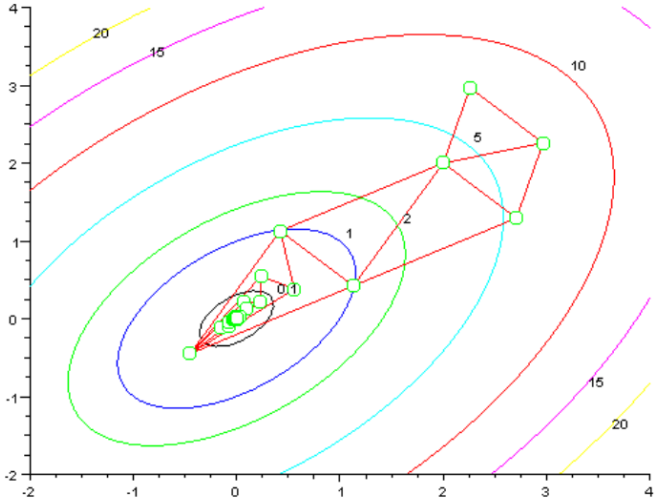

Fig. 3.7.: Movement of evaluation simplex in Nelder Mead algorithm. The algorithm starts in the upper right and moves towards the lower left, following the gradient of the coloured contour lines. [35]

contraction, moving closer to an optimal solution with every step. Figure 3.7 shows an example of the movement of the evaluation simplex towards the minimum in the solution space.

4 Method

This chapter describes the methods used in this thesis. We will start with the underlying workings of SRIM and the approach for the validation of its functionality. After this the implementation in Matlab and the Comsol simulation setup is described, followed by the design and fabrication of the microfluidic chips and the custom micro-particles. Finally the experimental setup is described.

4.1 General principles of SRIM

As stated in the background and the introduction, SRIM (shape reconstruction from impedance measurements) is an adaptation of a concept proposed by Vasilis Papadimitriou. In his concept, the shape of a non-conducting particle could be extracted with deconvolution from the measured impedance signal of the particle passing through a specially shaped channel. However, instead of using deconvolution, SRIM builds a system of equations and solves it with a computational optimizer. The underlying mathematics are described in the following section.

Figure 4.1 shows a channel with cross sectional slices A_C of equal thickness with an embedded object with slices A_O. The dimensions of the channel slices are known, while the dimensions of the object slices are what we are after.

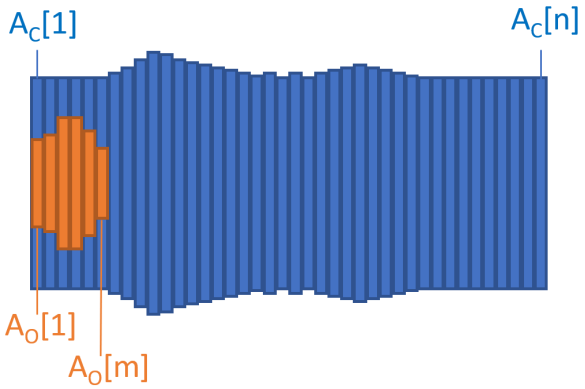

Fig. 4.1.: Division of object (A_O) and channel (A_C) in 'slices'

The areas of each slice are numbered as following:

$$A_c = \Big[A_c[1], A_c[2], A_c[3]...A_c[n]\Big] \tag{4.1}$$

$$A_o = \Big[A_o[i], A_o[ii], A_o[iii], ...A_o[m]\Big] \tag{4.2}$$

By converting equation 3.6 to a discrete form, it can be used to approximate the resistance of this configuration. This discrete form is given by equation 4.3, which is a function of the areas of each slice of both the object and the channel. When the object moves one step further into the channel, the function changes and we get a new value for the resistance, as shown in equation 4.4. So, by moving the object, we can build a system of equations and when the channel length is long enough relative to the object length, we are provided with enough equations to make this an overdetermined system of equations. This system can then be used to find the values of A_O.

$$R_0 = \frac{1}{A_c[1] - A_o[i]} + \frac{1}{A_c[2] - A_o[ii]} + \frac{1}{A_c[3] - A_o[iii]} + ... + \frac{1}{A_c[m+1]} + ... + \frac{1}{A_c[n]} \tag{4.3}$$

$$R_1 = \frac{1}{A_c[1]} + \frac{1}{A_c[2] - A_o[i]} + \frac{1}{A_c[3] - A_o[ii]} + ... + \frac{1}{A_c[m+2]} + ... + \frac{1}{A_c[n]} \tag{4.4}$$

Solving this system analytically however is problematic for two reasons: firstly, to have high resolution of the object under investigation, it is necessary to have many indexes for A_O, which will result in a large amount of equations and therefore high complexity of the system. Secondly, in practice, it will not be possible to measure values for R in each object position, such that the system will be consistent. For the system to be consistent, all equations should be valid for the same values of A_O. However, as measured values for R will at least contain a certain measure of noise, without even considering other sources of deviation, this cannot hold. For this reason, a computational optimizer is used to find a best fitting solution for the system.

4.1.1 Procedure for validation and application of the method

To confirm that SRIM can achieve its goals, its functionality must be validated. This is approached in two manners within this thesis. The first path is a qualitative approach, where the reconstruction results are compared to the input objects qualitatively. The approach advances through environments of increasing complexity in a stepwise manner. Figure 4.2 shows an overview of these steps and the additional complexities introduced in each phase. In the first step, a resistance profile of an object moving through a channel is generated using the Matlab

model, described in section 4.1.2, after which the optimizer uses the model to reconstruct the object shape. Next, the resistance profile is generated from a Comsol physics simulation, where the electric field is simulated using finite element simulation. This results in the Comsol simulation having current inhomogeneity similar to a real-life situation. The resulting resistance profile is once again fed into the model-optimizer combination and the results are judged qualitatively. Finally, physical experiments are conducted where the resistance is measured while the object moves through the measurement channel and the results of this are used for reconstruction and comparison.

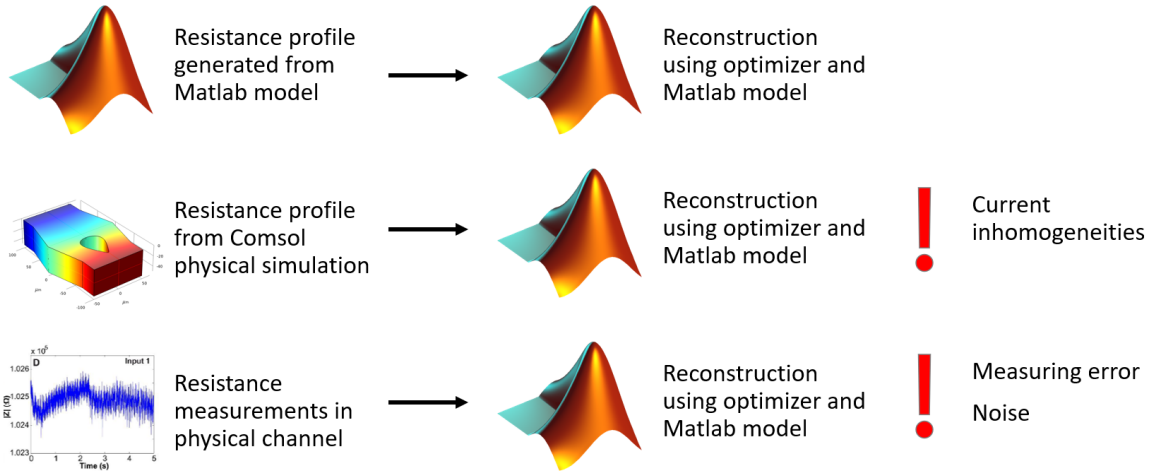

Fig. 4.2.: Steps of increasing system complexity in SRIM validation

Although the results can easily be compared quantitatively to the input objects, for example by taking the root mean square deviation, it was found that this did not always give a useful evaluation. Whether specific characteristics of interest are present in the reconstructed shape, can be more important than reduced overall deviation. For this reason, the first approach is a qualitative approach, where the results are not meant for direct comparison of performance, but rather as insights in the capabilities of the method.

In the second approach, simulation results of several different object shapes are used for a classification experiment, so as to also provide a quantitative measure. In this experiment, the simulated resistance profiles are compared with the resistance profiles generated by the model of several shape categories by means of minimal root mean square deviation.

4.1.2 Matlab resistance model

The resistance model is used to generate the resistance profiles. It starts with two variables containing the area in square meters of each slice of the object and the channel. Each slice

represents a slice of 1 μm, although this and the unit of area can be varied depending on the implementation.

$$\text{Object} = \begin{bmatrix} \text{Ob1} & \text{Ob2} & \text{Ob3} \end{bmatrix}$$

$$\text{Channel} = \begin{bmatrix} \text{Ch1} & \text{Ch2} & \text{Ch3} & \text{Ch4} & \text{Ch5} & \text{Ch6} \end{bmatrix}$$

The script then concatenates the object variable with zero values to make it the same length as the channel variable.

$$\text{Object\_filled} = \begin{bmatrix} \text{Ob1} & \text{Ob2} & \text{Ob3} & 0 & 0 & 0 \end{bmatrix}$$

The function *circshift* is then used to make an array of shifted versions of the channel. The first row is unshifted, the second row is shifted back 1 position, the third row is shifted back 2 positions etc. The channel shifting back, relatively, gives the same effect as the object moving forward.

$$\text{Channel\_circshift} \begin{bmatrix} \text{Ch1} & \text{Ch2} & \text{Ch3} & \text{Ch4} & \text{Ch5} & \text{Ch6} \\ \text{Ch2} & \text{Ch3} & \text{Ch4} & \text{Ch5} & \text{Ch6} & \text{Ch1} \\ \text{Ch3} & \text{Ch4} & \text{Ch5} & \text{Ch6} & \text{Ch1} & \text{Ch2} \\ \text{Ch4} & \text{Ch5} & \text{Ch6} & \text{Ch1} & \text{Ch2} & \text{Ch3} \end{bmatrix}$$

The object variable is then subtracted from each of the shifted channels, to calculate the resulting area in each slice.

$$\text{Channel\_circshift\_minus\_object} \begin{bmatrix} \text{Ch1}-\text{Ob1} & \text{Ch2}-\text{Ob2} & \text{Ch3}-\text{Ob3} & \text{Ch4} & \text{Ch5} & \text{Ch6} \\ \text{Ch2}-\text{Ob1} & \text{Ch3}-\text{Ob2} & \text{Ch4}-\text{Ob3} & \text{Ch5} & \text{Ch6} & \text{Ch1} \\ \text{Ch3}-\text{Ob1} & \text{Ch4}-\text{Ob2} & \text{Ch5}-\text{Ob3} & \text{Ch6} & \text{Ch1} & \text{Ch2} \\ \text{Ch4}-\text{Ob1} & \text{Ch5}-\text{Ob2} & \text{Ch6}-\text{Ob3} & \text{Ch1} & \text{Ch2} & \text{Ch3} \end{bmatrix}$$

The result is then inversed and summed for the modeled resistance at each shifted position, just as equation 4.3 and 4.4 describe for the starting and the first shifted positions. Because the elements of each row are eventually summed, their order does not matter.

For practical applications, several other steps and factors are implemented as well, like object and channel conductivities, size scaling and input voltage.

The script of the Matlab file containing the resistance model can be found in appendix B.1.

4.2 Object design

Two shape characteristics were chosen to evaluate the ability of the SRIM method to resolve sperm morphology characteristics. These were ridges in the object and asymmetry of the object. The shapes that resulted from this are shown in figure 5.3. Additionally, several 2D shapes were used during the development of the SRIM script, among which a spermlike object. These were not all converted to 3D shapes in the COMSOL physics simulations however due to time constraints.

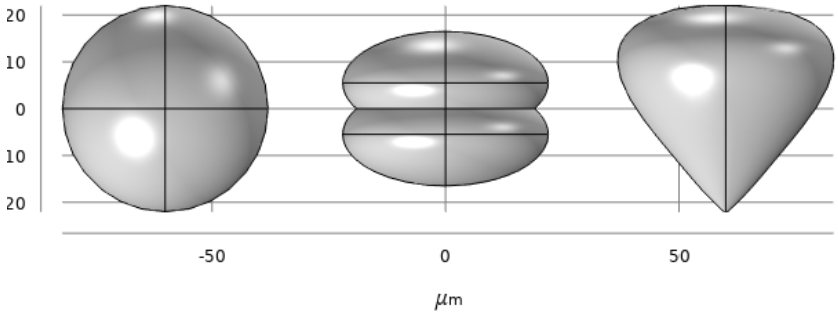

Fig. 4.3.: Overview of the object shapes used for SRIM evaluation.

4.3 Matlab optimizer

The optimizer script tries to find values for the object slices to best match the provided resistance profile. As explained earlier in section 3.4, one of the ways to implement optimization is the minimisation of a given cost function. In our case the cost function is based on the summed square of the deviation between the given (measured or simulated) resistance profile and the resistance profile that is generated in our model from a proposed object. The variable that will contain the proposed object is referred to as x.

The function *fmincon* is used to implement the optimization. It is the constrained version of *fminsearch* and also uses the earlier discussed Nelder-Mead simplex algorithm. The constraints that are set are based on physical constraints that the examined object has to adhere to. The currently implemented constraints include the dimensions of the tightest part of the channel as upper bound to the value of the object slices and 0 as the lower bound. In other words,

the object slices cannot be larger than the tightest part of the channel and they cannot be of a negative size. If information about the examined objects is available, further constraints could be implemented.

fmincon requires a starting value for the proposed object. This indicates the point in the solution space where the optimizer will start. Initially, in my implementation, this point was always set at the null vector, however, this will in theory bias the optimizer towards solutions that are closer to this point. Due to this bias, if any information is present about the unknown objects, this can be processed in the starting value to improve the results of the optimization.

fmincon provides access to many more parameters, besides the ones that are mentioned before. Several of these were used to tweak the processing time and the solution quality by respectively limiting the total amount of function evaluations and lowering the satisfactory boundary for the cost function, called the tolerance. At an earlier point of development, a scalar was used to increase the cost function so that the algorithm would converge further towards a solution. In theory, this should have functioned identically with decreasing the tolerance, but in practice, results differed. This could be caused by factors in the internal implementation of *fmincon*.

Regularisation was applied when the result of the optimization showed overfitting, resulting in a solution with many sharp peaks. Regularization was implemented by adding a smoothness cost defined as function h(x) on line 163 of appendix B.1.

4.4 COMSOL simulation

The COMSOL model is a simplified model of the experimental setup. The only parts modeled are the liquid in the microfluidic channel and the suspended object in the channel. The conductivity of the liquid can be set to a value that reflects experimental values, i.e. 1 Sm^{-1} for a 0.9% NaCl solution or up to 20 Sm^{-1} for highly concentrated 21.9% NaCl solution. The conductivity of the examined object can also be set to a value that reflects the material choice of the object, like polystyrene, of which microbeads are often made of.

The voltage source was modeled in two different ways. The first model (shown in figure 4.4a) reflects the physical setup, where the electrodes are of the sames size as they would be on the chip and are embedded in the bottom of the channel. Furthermore, the distance between the electrodes and the broadening or narrowing part of the channel are also set at such a value that the electric field is expected to have homogeneously dispersed over the height of the channel for the most relevant parts of the channel, akin the liquid electrode design. The sharp direction change that the current lines have to go through due to the perpendicular orientation of the electrodes to the current direct, required a very fine mesh for correct results. Several simulations

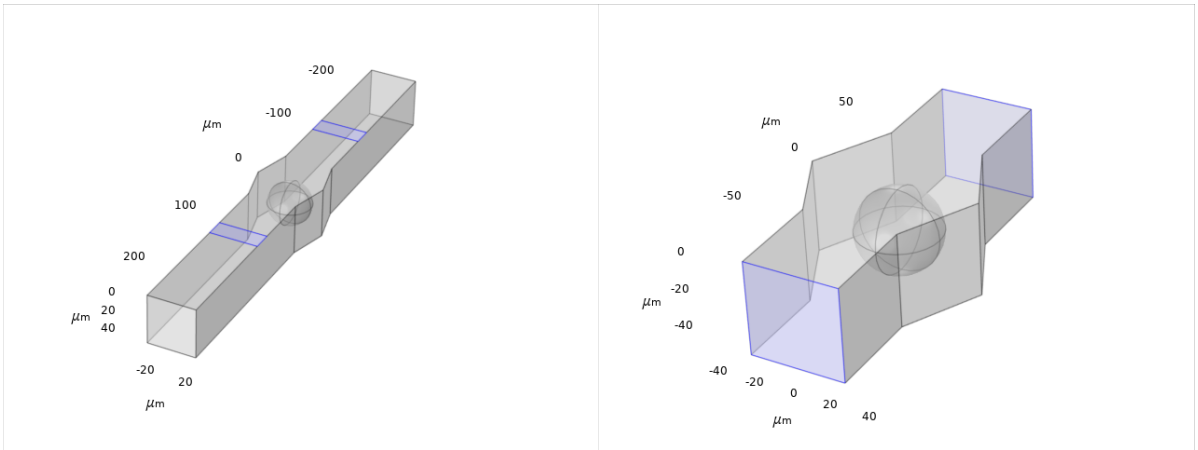

(a) First complete model (b) Second simplified model

Fig. 4.4.: The two used COMSOL models. The virtual electrodes are highlighted in blue.

were run where the workings of the setup were examined, but this was an unsuitable model to carry out extensive examinations.

The second model (shown in figure 4.4b) assumed the dispersion would take place correctly and that a particle in part of the channel with the homogeneous field distribution would only minimally affect the field distribution in the dispersion zones. It therefore modeled a shorter segment of the channel and had its virtual electrodes placed over the full height at the two ends of the channel. Additional models were used to examine the electric field distribution in the liquid electrode setup and confirm if the distribution occurred within the distance reported in the literature. The voltage source in the model was a DC voltage source.

Movement of the objects was simulated by changing the object position and running a simulation for each position.

4.5 Chip design

To fabricate the chips, first a lithography mask is made, which is then used for positive lithography in SU-8. The resulting wafer can then be used as a master to produce PDMS chips. This section describes the design process for the lithography mask, which ultimately results in the channel shapes. The chips were designed with three aspects in mind: a channel profile that varies in cross sectional area as to provide an impedance signal, creating the optimal signal to noise ratio by minimizing both length and cross sectional area, and the reuse of existing materials.

The construction of the chip consists of a glass plate with electrodes, bonded to a PDMS chip with embedded fluidic channels. The glass chips are reused from earlier research and are reused. The electrodes consist of sputtered platinum which run in opposing, parallel fingers with varying spacing, as seen in figure 4.5 and the accompanying table 4.1 with the spacing distances. The glass chip is soldered onto a chip holder, which is a PCB with headers to facilitate electrical connection to the chip.

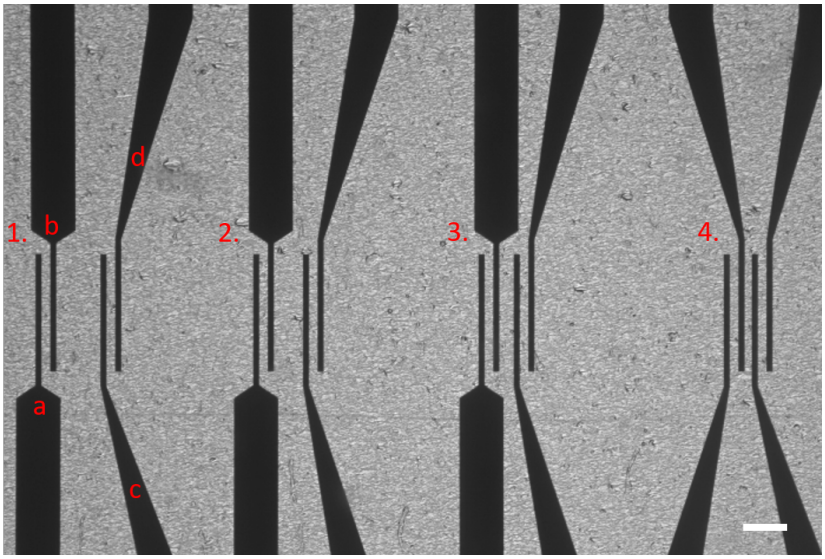

Fig. 4.5.: Electrode layout on glass slide. 4 sets of electrodes with decreasing distance between the middle electrodes. Letter labeling for sets 2, 3 and 4 is continued from left to right as is shown for set 1.See table 4.1 for distances between the different neighboring pairs.

Tab. 4.1.: Spacing between the electrode pairs. See figure 4.5 for the electrode layout. Each electrode is 20μm wide.

Pair	**Distance** (μm)
a-b	30
c-d	30
1 b-c	150
2 b-c	100
3 b-c	50
4 b-c	25
1d-2a	490
2d-3a	570
3d-4a	685

The channel profile of the chip was based on designs which performed well in simulations. The base design (shown in figure 4.6) has a widening taper, which is followed by a closing taper. The taper increases the channel area by 80% at its widest point and grows at a ratio of 1:1,

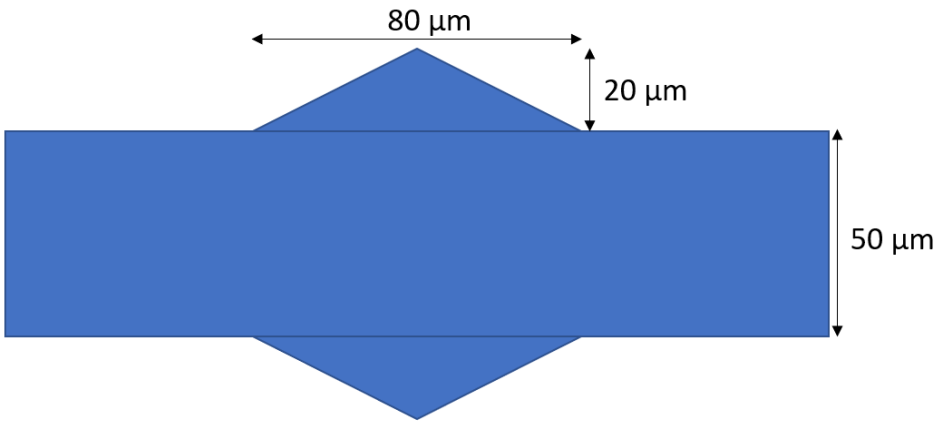

Fig. 4.6.: Design of base SRIM chip

meaning it widens 1μm for each μm in the axial direction. This ratio tries to strike a balance between changing the channel profile to give more impedance signal variation and smoothing out current density inhomogeneities caused by the varying channel size. Multiple variations based on this design are included on the same mask. These variations include size variation for test objects in different size ranges, shape smoothening variation between a straight taper and a taper based on a sine wave and inversed shape variation with a tightening channel instead of a broadening channel.

The chip shapes were designed for three size ranges: 50, 10 and 8 μm. The 50 μm wide channels were designed for initial proof of concept measurements with large beads and custom objects. The 10 μm and 8 μm wide designs were designed for small beads and sperm cells. The 8μm design is meant to increase signal strength but runs increased risk of clogging.

To further increase relative signal strength, the chips are designed to make use of differential measurement. By using two exactly equal measuring paths, where only one path undergoes a change which is to be measured, the signal of the two paths can be subtracted from each other. This eliminates any noise that is common in both measuring paths, increasing the signal to noise ratio. See figure 4.7 for illustration of the concept. The electrode pairings 1 b-c and 2 a-c for example are two pairs which span the same distance and can therefore be used for differential measurement. However, it must be noted that with the used electrode configuration, this will result in intermediate floating electrodes and parallel paths between electrodes which may lead to parasitic capacitance.

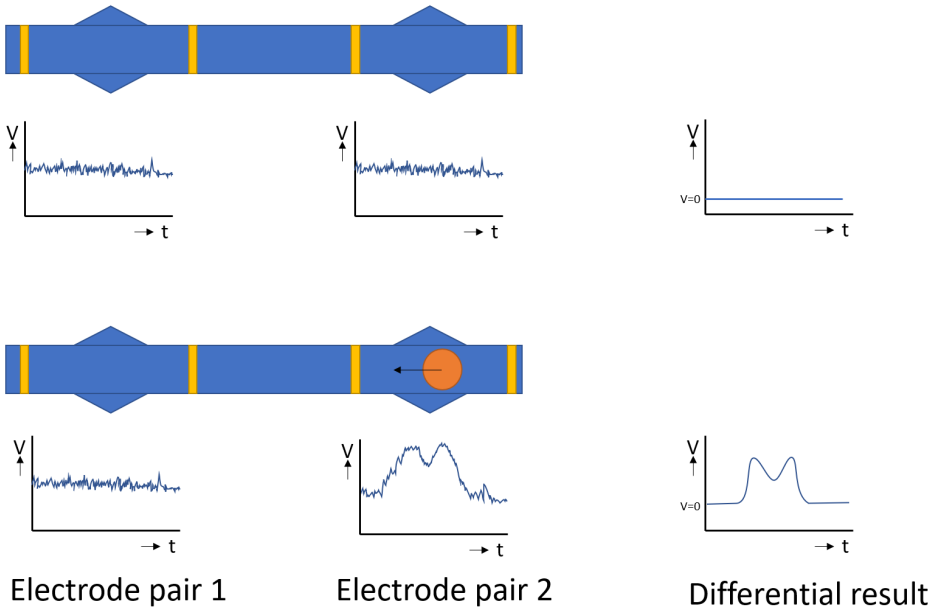

Fig. 4.7.: Illustration of noise reduction due to differential measurement.

4.6 Chip fabrication

The production process of the microfluidic chips involves the casting and curing of PDMS onto a silicon-SU-8 master wafer and the subsequent preparation and bonding of the chips to the glass chips. The fabrication of the master wafer is carried out in the clean room. The procedure for this is described in appendix C.4. The casting, curing and bonding are described in the protocol in appendix C.1 and C.2. Variations in this last protocol are shortly described in the following section.

The first important variable is the plasma treatment time and method. By increasing plasma treatment time, one can ensure stronger bonding between the glass and PDMS by increasing the amount of created silanol groups. Additionally, the glass can be treated as well to increase the amount of available silanol groups on the glass surface through activation of the silicon and cleaning of the hydration layer. Weak bonding will lead to chips which are susceptible to loosening, which can lead to leakage, during experimental procedures where perpendicular force is exerted on the chip, like during resuspension of fluids. When the chip is bonded too strongly however, removal of the PDMS chip from the glass slide can become difficult and may result in chunks or a layer of PDMS that stays stuck to the slide. These remains require chemical treatment to dissolve and remove them or they might cause problems during subsequent reuse. By leaving the PDMS or glass exposed to the atmosphere, its reactivity is reduced, which can be used to find the right balance in bonding strength.

Alignment of the microfluidic chips to the glass slides carrying the electrodes was done using a custom alignment tool that was designed for Bjorn de Wagenaar's research and is currently in use by Douwe de Bruijn. This tool has a free moving XYZ stage with four needles that can hold the PDMS chip. Alignment precision for this tool is approximately 10 μm.

4.7 Particle design and generation

Standard microbeads were used from inventory in the size 5 and 6 μm and additionally ordered in the size 45 μm.

In order to test the functionality of the method, custom particles were required with controlled shape variations. As the required shapes, e.g. cones, were not commercially available, it was chosen to produce these in our in-house cleanroom. The process is described in the protocol in appendix C.5. The process is similar to the fabrication of the master wafer, except that the SU-8 is soaked in a solvent so that it releases from the wafer. Due to this same process, the particle also receive the same shape profile: the top face follows the mask shape, while the side edges will have slight taper due to light diffraction underneath the mask.

The 2D shapes contain characteristics that were chosen as benchmark characteristics for cell morphology identification, including tapering and ridges. Additionally stars and hearts were added arbitrarily as there was additional space on the wafer.

Additionally, contact was made with the research group of Dr. Burak Eral of the TU Delft. His group makes use of a stop flow lithography setup [36], which is able to produce 2D shapes from hydrogels, but which is more limited in the height of the particles.

4.8 Microfluidic experimental setup

Setup and settings

The constructed microfluidic chip was connected in a setup shown in figure 4.8. The CETONI neMESYS syringe pumps provided suction for pressure driven flow and operated 0.5 μL min^{-1} for the 50 μm channels and at 0.007 μL min^{-1} for the 8 and 10 μm channels. The Zurich Instruments HF2LI impedance spectroscope equipped with a HF2TA current pre-amplifier was used to record the impedance across the SRIM channel. A 100kHz sinusoidal output signal at an amplitude of 2V for the 50 μm channels and 10V for the 8 and 10 μm channels was generated on the output electrode. The frequency for this signal was chosen after device characterisation, as

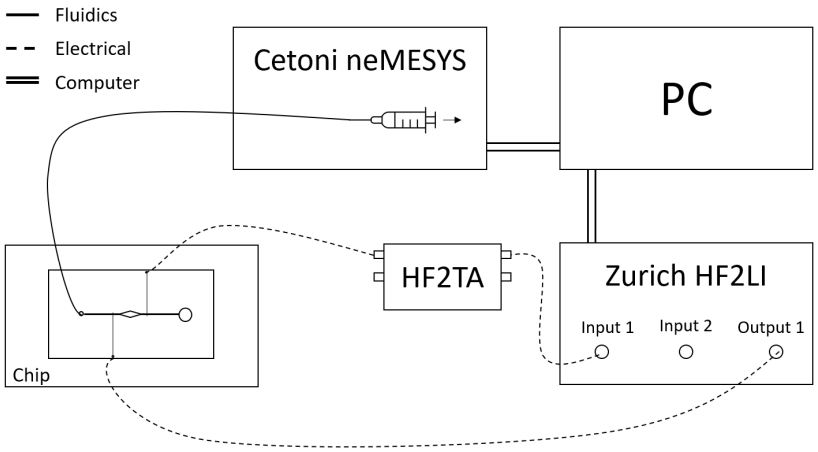

Fig. 4.8.: Experimental setup (adapted from [5])

described in section 5.4.1. The sensing electrode was used to measure the current through the channel, which was passed through a fourth order 2kHz low pass filter at a sampling frequency of 1.8kHz for the 50 μm channels and 14.4kHz for the 8 and 10 μm channels. At several points, experiments were run with higher sampling frequencies, but this was not deemed required for successful reconstruction. The output of the HF2LI was processed using the equations described in 'Characterization of electrically active defects at III–N/dielectric interfaces' by Roberta Stradiotto [37].The experiments were recorded with either a Olympus IX 51 or Leica DM IRM microscope equipped with a FLIR Grasshopper 3 camera recording at 163.3 frames per second.

Electrode setup

Initially, the chips were designed for a differential electrode setup. This required two identical electrical paths with with the object under investigation running through one of the two paths. A higher signal to noise ratio could be acquired by subtracting the two signals from each other. By using the existing electrode layout however, one pair of electrodes had its electrodes running parallel, while the other pair had its electrodes coming from opposite sides. This caused an offset in the impedance due to the parallel electrodes having a higher amount of parasitic capacitance. Furthermore, it was discovered that the floating electrodes which were present in the paths for differential measurements caused too much distortion of the signal. Instead, a single electrode pair, free of any floating electrodes in between them, was used around the SRIM channel of interest.

Sample and chip preparation

The polystyrene beads and SU-8 custom particles were suspended in a 0.9% NaCl solution with a conductivity of 1.372 Sm^{-1} for electrical contrast. The concentration of the 0.9% NaCl solution was chosen as it is approximately isotonic to human blood and was therefore deemed physiologically normal for the sperm cells. The 45 μm beads were diluted to a concentration of $1,0 \cdot 10^4$ particles/mL. The exact concentration of the custom particles is unknown, but appeared to be slightly lower than the 45 μm beads. The sperm cells were diluted to approximately $2 \cdot 10^6$ cells/mL and 5 or 6 μm beads were added in a 1:4 ratio to the sperm cells.

In order to reduce tumbling caused by shear forces, the SU-8 custom particles were suspended in 21.9% NaCl solution with a conductivity of 18.61 Sm^{-1}. This solution has an increased density compared to the 0.9% NaCl solution to compensate for the density difference between SU-8 and the electrolyte.

Before every experiment, the microfluidic chips were tested for leaks using demineralised water coloured with food dye. After passing this examination, the chips were rinsed with PLL-PEG for at least 15 minutes to prevent object and cell adhesion to the channel walls.

4.9 Simulated classification experiment setup

As the quality of the reconstruction results is difficult to evaluate objectively, a simulated classification experiment is added. In this experiment, it is evaluated if the SRIM method is able to identify one out of three possible object shapes from a simulated resistance profile. This is done by computing the cost function for each of the three objects with for a resistance profile and selecting the object with the lowest cost function. Regularisation cost was disabled, but the constant factor and the profile cropping were performed with the following parameters: $c_{constantcorrection} = -4.5 \cdot 10^3$ and cutting of the outer 20 μm of positions in the resistance profile at both ends. The $c_{constant}$ value was slightly lowered compared to the value used in the shape reconstructions from the COMSOL profiles. This change increased classification performance.

Additionally, offset positioning in the height and in the long axis of the channel were added to increase the variation in the resistance profiles. The position variations of the objects were 0 to 1.5 μm offset in the height in steps of 0.5 μm and 0 to 10 μm to the front or back in the step 1, 3, 5 and 10 μm. As the SRIM model generates its resistance profiles with a centered object, these offsets in the COMSOL resistance profiles test the classification method for robustness against differences in the expected object position.

5 Results

This chapter presents the findings of the research done in this thesis. Following the work flow presented in the method, the results are presented in increasing order of system complexity. First, the accuracy of the model is determined by comparing model results with manual calculations and finite element methods physics simulations. Subsequently, the reconstruction by the optimizer is tested with resistance profiles of moving objects generated by the model and by physics simulations. Finally, experimental measurements are compared with simulated values and a reconstruction is attempted from the measured data. **Classification experiment**

5.1 Resistance comparisons between SRIM model and COMSOL simulations

First, we compare the resistance values generated by the model of static geometries with the values from manual calculations and COMSOL physics simulations, followed by comparisons of resistance profiles of moving objects.

5.1.1 Empty channels

We start with the comparison of resistance calculations of channels filled with only electrolyte and without suspended objects. We do this in the setup shown in figure 4.4b. The channels we use for this are a cylindrical channel[1] (figure 5.1a), whose resistance can be verified with a manual calculation and one channel specially shaped for SRIM [2](figure 5.1b).

Tab. 5.1.: Resistance value comparison between COMSOL physics simulation, model and manual calculation for cylindrical and SRIM channel

	COMSOL value (kΩ)	Model value (kΩ)	Manual calculation (kΩ)
Cylinder	25,464	25,464	25,464
SRIM channel	64,783	63,512	-

[1]Dimensions cylindrical channel: r=50μm, L=200μm, σ=1Sm^{-1}.
[2]Dimensions SRIM channel: $W_{straight}$=50μm, W_{widest}=90μm, h=50 μm, L_{total}=180μm, $L_{widening}$=80μm, σ=1Sm^{-1}

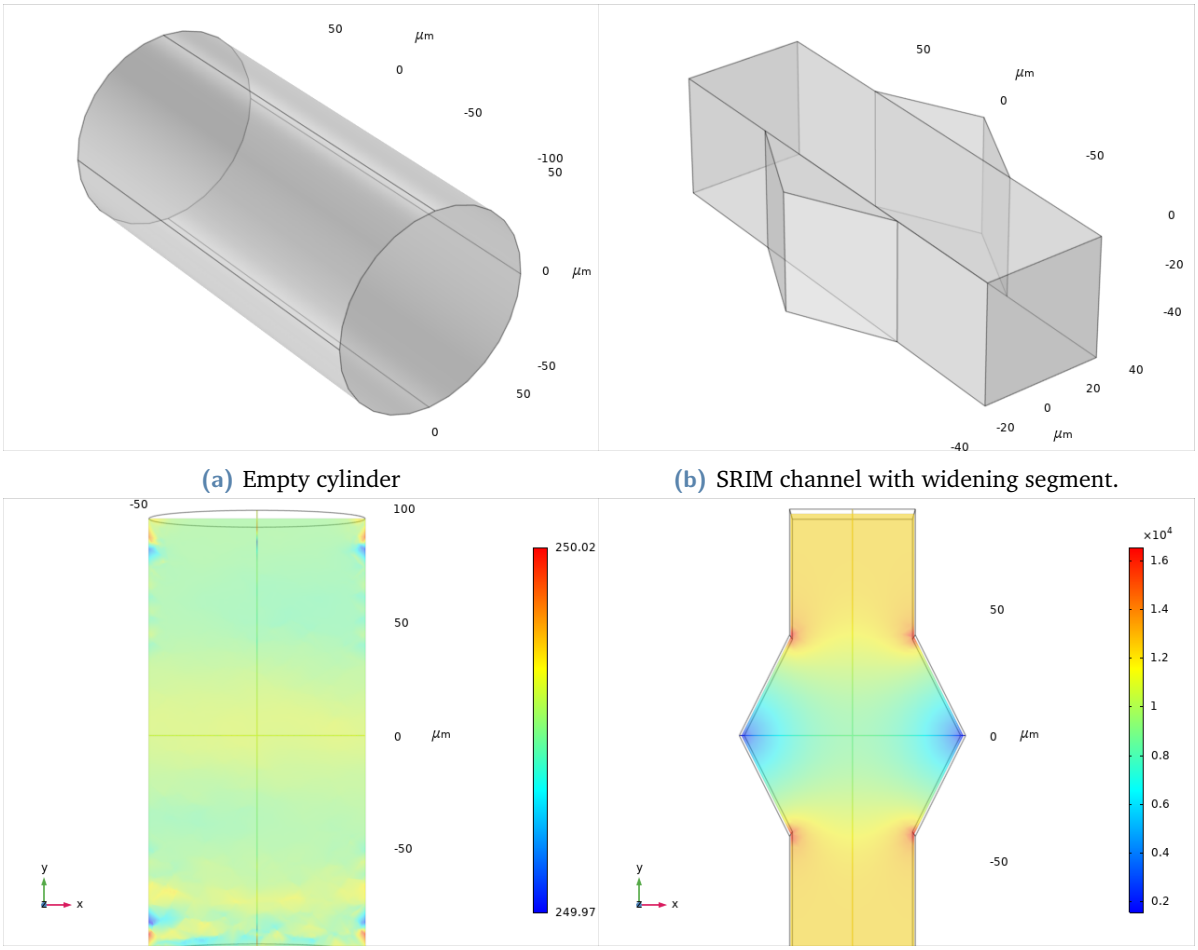

(a) Empty cylinder

(b) SRIM channel with widening segment.

(c) Current density in the cylinder.

(d) Current density in the SRIM channel.

Fig. 5.1.: Comparison of current density distribution in a cylindrical channel and the SRIM channel. Note the small range in the scale bar of the cylindrical channel, compared to the SRIM channel.

Table 5.1 shows an overview of the simulated resistance for both geometries and the resistance values predicted by the model and by manual calculation. In the cylindrical channel, the current distribution is completely homogeneous, as shown in figure 5.1c, due to which the model is able to accurately predict the resistance of the channel. Figure 5.1d shows the SRIM channel, in which the current distribution is more inhomogeneous, which leads to a 1.9% lower value of the resistance in the model compared to the physics simulation.

5.1.2 Spheres of different sizes in cylinder

To evaluate the accuracy of the model for different object sizes, non-conducting spheres of different sizes were simulated in a conducting channel. Table 5.2 shows the resistance values for each sphere suspended in the channel. The total resistance in the cylinder can be seen as

the sums of the resistance of the empty cylinder and the additional resistance that is caused by the required field distortion needed to bypass the sphere. To more accurately compare the calculation of this second part, table 5.3 shows the resistance values with the resistance of the empty cylinder subtracted. The model consistently underestimates the resistance caused by the sphere, as it does not take the added resistance caused by current inhomogeneity into account. From literature [22][26], it is expected that the accuracy of the model increases as the object size grows, relative to the channel size. This is because larger objects lead to a slower change in geometry as described in section 3.2. This effect can be seen in table 5.3. Furthermore, although the geometrical setup is identical to the setup described in DeBlois and Bean's 1970 paper[22], the resistance difference between the COMSOL physics simulation and the model results is different from the deviation for which DeBlois and Bean proposed their correction due to the different calculation approaches.

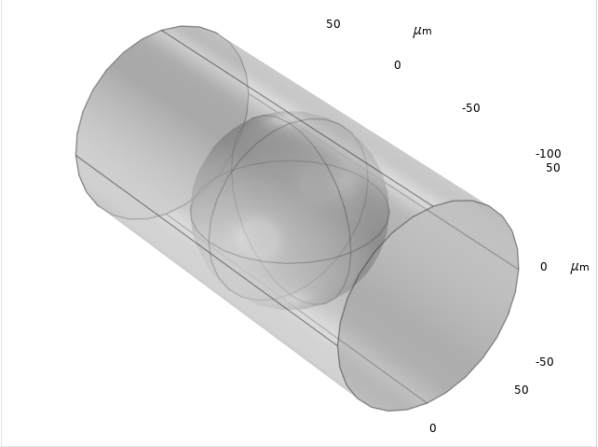

Fig. 5.2.: Configuration for resistance determinations of differently sized spheres in cylindrical channels in COMSOL physics simulation.

Tab. 5.2.: Comparison of resistance values for spheres of increasing size in a cylindrical channel.

Sphere radius (μm)	COMSOL resistance (kΩ)	Model resistance (kΩ)
10	25.567	25.531
20	26.323	26.073
30	28.787	28.023
40	36.610	34.837
45	49.191	46.477

Tab. 5.3.: Comparison of differential resistance caused by the embedded object, where the resistance value of the empty channel is subtracted.

Sphere radius (μm)	ΔR COMSOL (Ω)	ΔR model (Ω)	Underestimation
10	102	67	35%
20	858	608	29%
30	3 322	2 558	23%
40	11 145	9 372	16%
45	23 700	21 013	11%

5.1.3 Moving objects in shaped channel

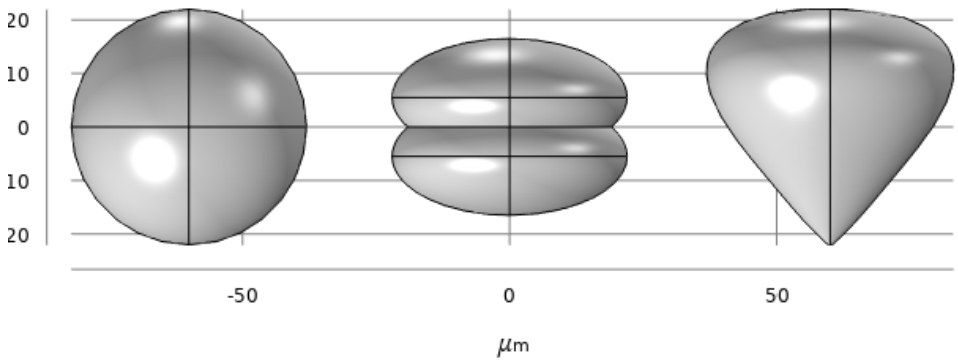

Fig. 5.3.: Overview of objects used in COMSOL physics simulations. Left to right: 44μm sphere, fused ellipsoids and skewed ellipsoid.

Next, the resistance profile of a moving object is generated in both the model and in the COMSOL physics simulation. The used channel has the same dimensions as mentioned in section 5.1.1. The particle centre moves in steps of 1μm from 60μm before the widest point of the channel until 60 μm behind the widest point of the channel. Figure 5.3 shows the objects examined in the physics simulations.

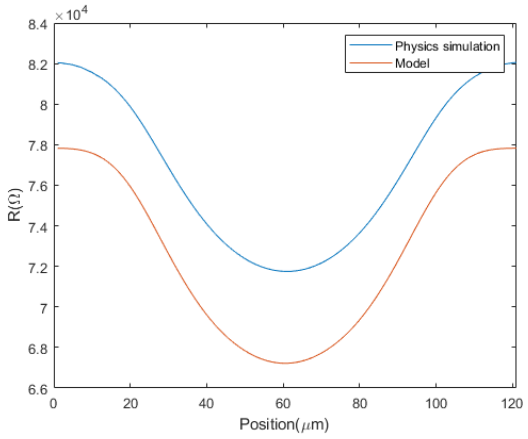

(a) Resistance profiles sphere

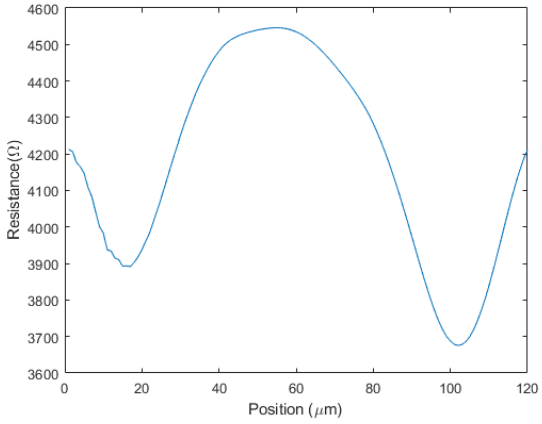

(b) Difference model and simulations sphere

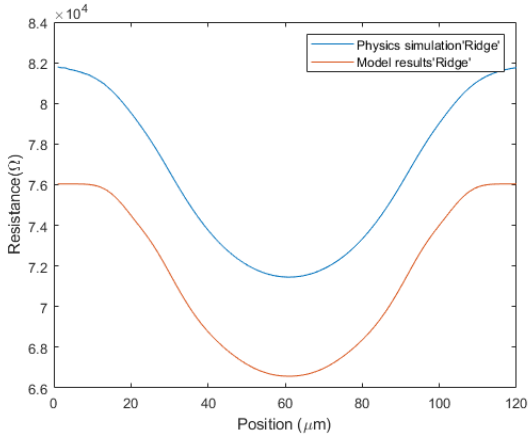

(c) Resistance profiles fused ellipsoids

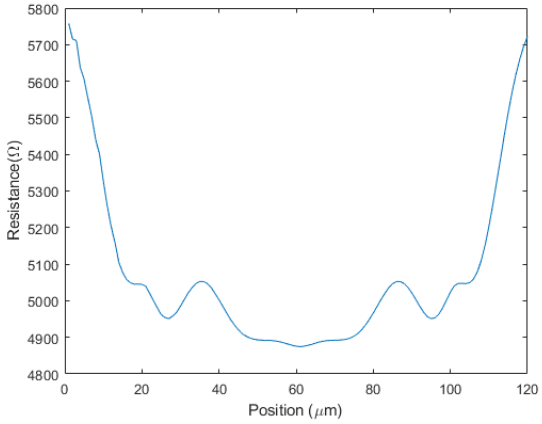

(d) Difference model and simulations fused ellipsoids

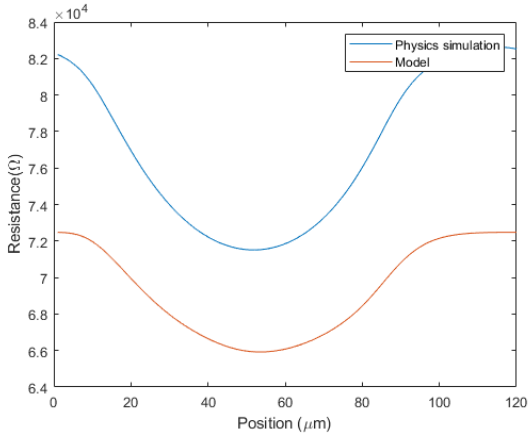

(e) Resistance profiles teardrop

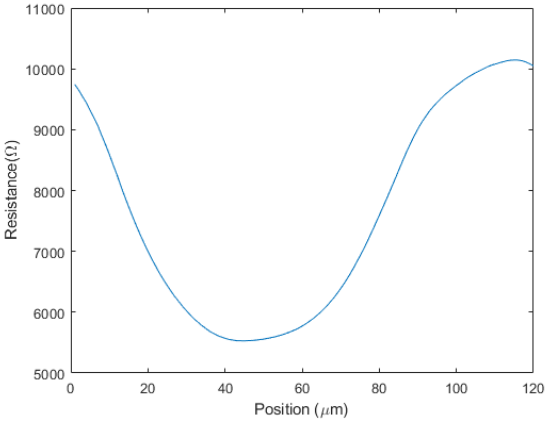

(f) Difference model and simulations teardrop

Fig. 5.4.: (a)(c)(e) Resistance profiles of objects moving through a SRIM channel as generated in the model and in a COMSOL physics simulation. (b)(d)(f) Difference between the resistance profiles shown in figures (a),(c) and (e).

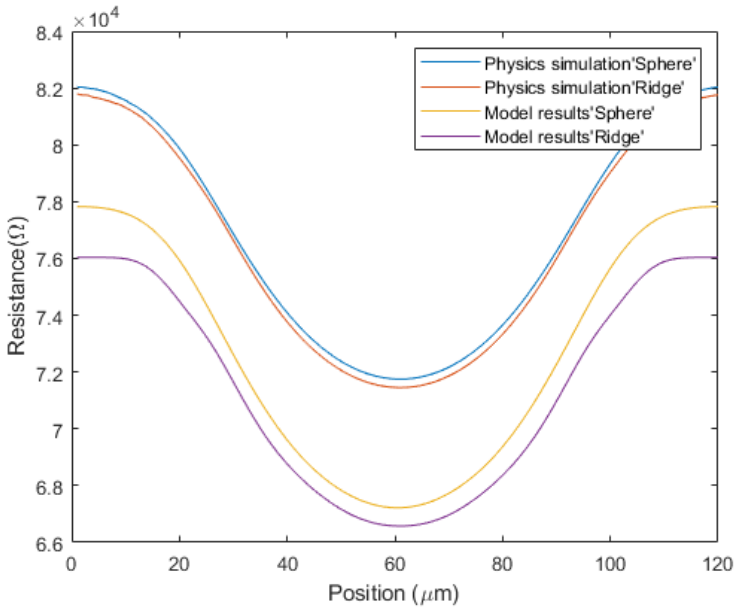

Fig. 5.5.: COMSOL physics simulation results and model results compared for the 44μm sphere and the fused ellipsoid particle.

Figure 5.4a shows the resistance profiles of a 44μm sphere moving through the SRIM channel. Figure 5.4a and 5.4b show how the model underestimates the resistance at all points in the channel, varying between 4.6% underestimation and 6.3% underestimation. The difference appears to be asymmetrical with regards to the distance to the middle of the channel, which is unexpected, but might be caused by meshing irregularities in COMSOL.

Figure 5.4c shows the resistance profiles for the particle composed of two fused ellipsoids. The profile generated by the model is similar to the profile generated by the COMSOL physics simulation, but once again consistently underestimates the value, this time between 6.3% and 7.0%. The distribution of the underestimation is quite different however. The asymmetry of this profile is lower than for the profile of the sphere.

When the profiles of the two objects are compared, as seen in figure 5.5, the resistance profiles as generated by the COMSOL physics simulations appear quite similar to the naked eye, with a minor and apparently constant difference, which might be caused by the difference in volume. The model resistance profiles are similarly close to each other for the two particles, but have an increased difference between them when compared to the simulation results.

The resistance profile for the teardrop particle is shown in figure 5.4e. Once again the resistance is underestimated by the model, but to a much larger degree then for the other two particles, as seen when figure 5.4f is compared with figure 5.4b and figure 5.4d. The magnitude of the deviation in the middle sector is comparable with the other two objects, but the deviation on the sides is almost twice as high. The asymmetrical nature of the particle is reflected in

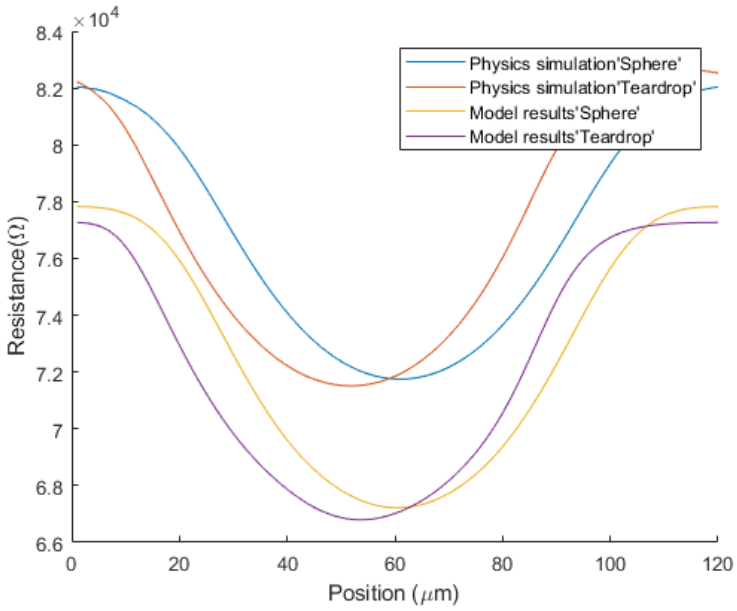

Fig. 5.6.: COMSOL physics simulation results and model results compared for the 44μm sphere and the teardrop particle.

an asymmetrical resistance profile. This can be seen better when the resistance profile of the teardrop particle is compared with that of the spherical particle in figure 5.6.

5.2 Shape reconstruction results

In the previous section we have compared the resistance profile predictions from the SRIM model to the COMSOL physics simulation results. In this section, the SRIM model is combined with the computational optimization algorithm to reconstruct the object shape from the provided resistance profiles.

5.2.1 Shape reconstruction from model resistance profiles

Figures 5.7a and 5.7b show the results of the object reconstruction using computational optimization from an impedance profile generated in the Matlab model.

Figures 5.7a and 5.7b show the results for two 2D versions of shapes that have been used in the simulations as benchmarks for relevant characteristics. In the appendix A, figure A.2a shows the area of the cross sections of a 3D sphere. Figure A.2b shows the 2D side view of the same sphere, by assuming each slice of the object is round and converting the area of the circle to its diameter.

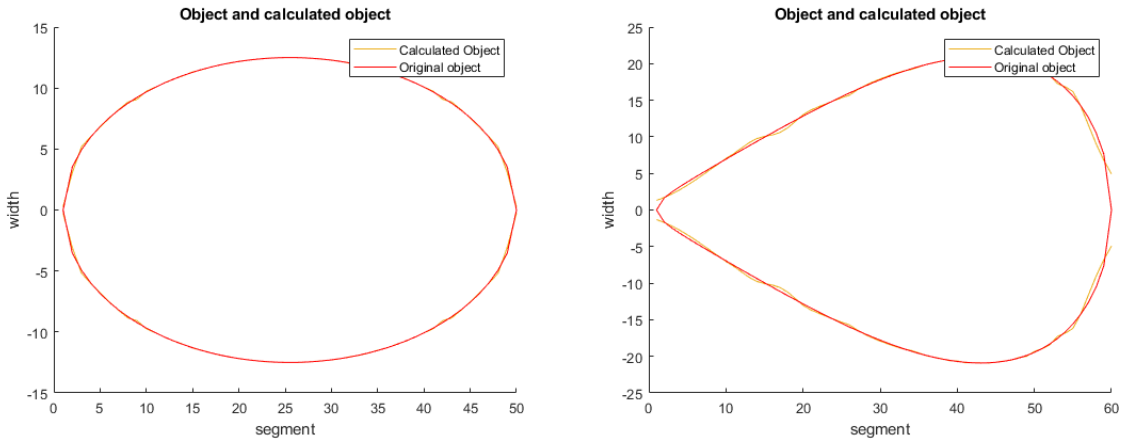

(a) Circle (b) Teardrop

Fig. 5.7.: Reconstructions made with the Matlab SRIM script from resistance profiles made using the same script.

The orange line from the reconstructed object can in most cases not be distinguished from the red line of the original object. This shows how the optimizer is able to retrieve the original object dimensions from the resistance data.

5.2.2 Shape reconstruction from COMSOL physics simulation resistance profiles

Figure 5.8a shows the reconstruction result from COMSOL simulation data of the 44μm sphere in the SRIM. The reconstruction is able to trace the shape of the middle of the object, but has large widening sidelobes in front of and behind the object.

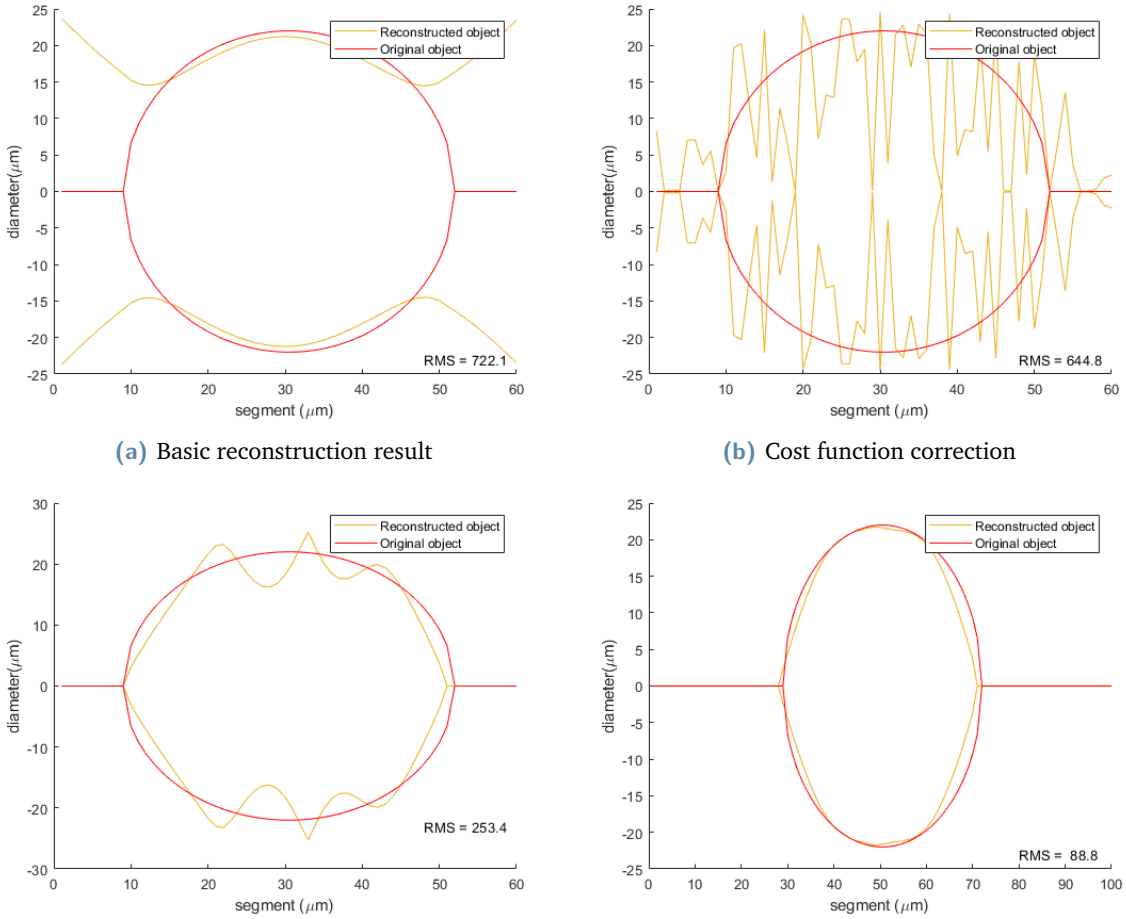

(a) Basic reconstruction result

(b) Cost function correction

(c) Additional smoothing regularisation

(d) Additional resistance profile cropping

Fig. 5.8.: Reconstruction results from the simulated resistance profiles of a 44 μm sphere. (c) features regularisation in addition to cost function correction and (d) also features cost function correction and regularisation besides introducing resistance profile cropping.

In section 5.1.3, it was shown that the resistance profiles generated by the model and by the physics simulations had a relatively consistent difference around 7% of the total value. To prevent that the shape reconstruction is going to compensate for this difference by adjusting the object shape, a constant value of $C_{correction} = 5 \cdot 10^3$ is subtracted from the cost function. This value is chosen as it lies around the average deviation of the different tested objects, thus bringing the model values closer to the simulation values for the multiple different objects.

Figure 5.8b shows the reconstruction result of the 44μm sphere with the constant correction value. The reconstructed object is very jagged, but its size approximates the original object and the sidelobes have been reduced. The curvature of the object however cannot be distinguished. Note that the horizontal red lines on the sides represent areas of 0 value.

To improve the reconstruction result, regularisation is applied. It is known beforehand that the objects used are relatively smooth and therefore a smoothness parameter is added to the cost function. Figure 5.8c shows the reconstruction result after smoothing regularisation. It can be seen that the object is already smoother, but still shows some ridges that should not be there. Further improvement of the reconstruction can be achieved by reducing the length of the used resistance profile by a third. This removes the sides of the resistance profile that produce the largest deviations in the corrected cost function. Figure 5.8d shows the reconstruction result after cropping of the resistance profile. The reconstructed shape is now recognizable as the original sphere, displayed as an ellipse in the figure due to 2D conversion and uneven axis scaling.

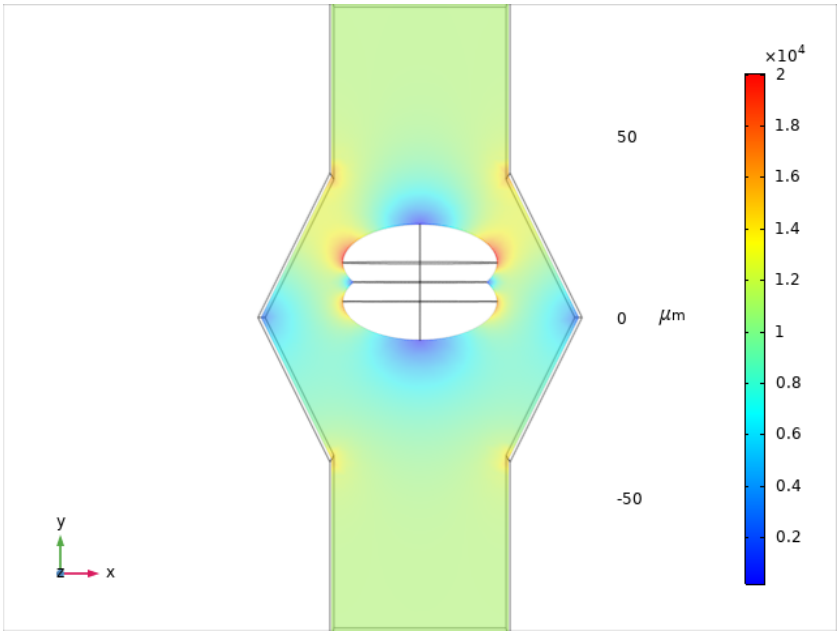

Fig. 5.9.: Current density around the fused ellipsoids pair. Around the ridge that connects the two ellipsoids a small region of low current density can be seen.

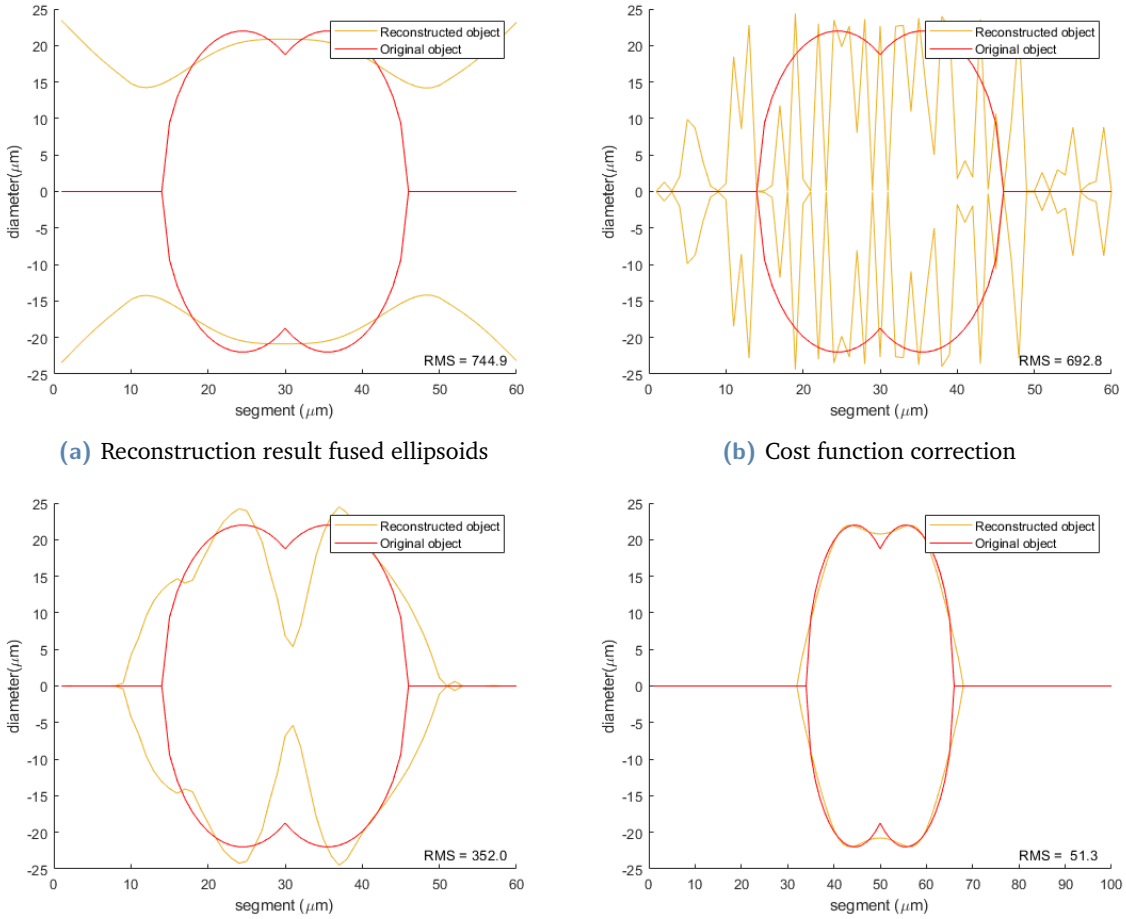

(a) Reconstruction result fused ellipsoids

(b) Cost function correction

(c) Additional smoothing regularisation

(d) Additional resistance profile cropping

Fig. 5.10.: Reconstruction results from the simulated resistance profiles of the 44 μm fused spheroid particle. Addition of the correction steps occurs identically to figure 5.8

To see if these corrections do not create a bias to a sphere shaped solution, figures 5.10a up to 5.10d show the reconstruction results for the object composed of fused ellipsoids with the exact same correction constant, regularisation function and profile cropping. 5.10d again shows an approximation of the object shape with large sidelobes. The ridge between the two fused ellipsoids is not visible in this reconstruction. When the correction constant is added in figure 5.10b, the sidelobes are reduced, but the result is very jagged again. By adding regularisation (figure 5.10c), the jaggedess is removed and the original object becomes recognizable. Interestingly, the ridge between the two ellipsoids is exaggerated and the object is slightly wider in this reconstruction. Cropping the resistance profile to the central two thirds once again removes the parts of the profile with the highest deviation and the reconstruction in figure 5.10d undergoes further improvement from this step. Although the ridge is visible, it must be noted that it shallower than in the original object. Figure 5.9 shows that the current density in the ridge is lower than in the surrounding channel. Therefore the electrolyte in this

ridge contributes to the conductance to a lower extent and the ridge is therefore less visible in the reconstruction.

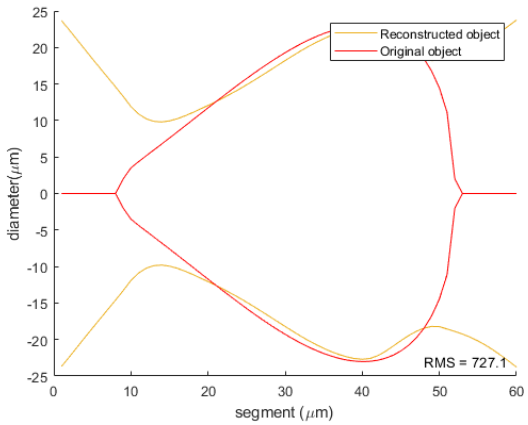

(a) Reconstruction result teardrop

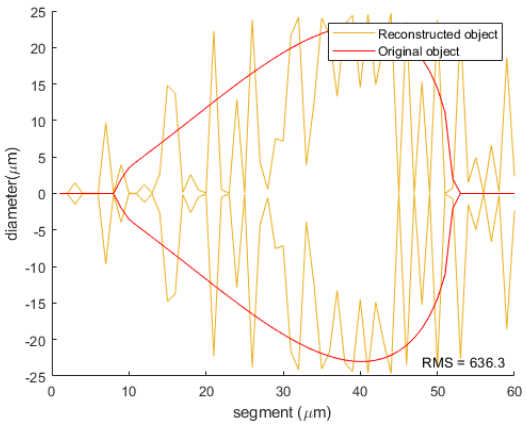

(b) Cost function correction

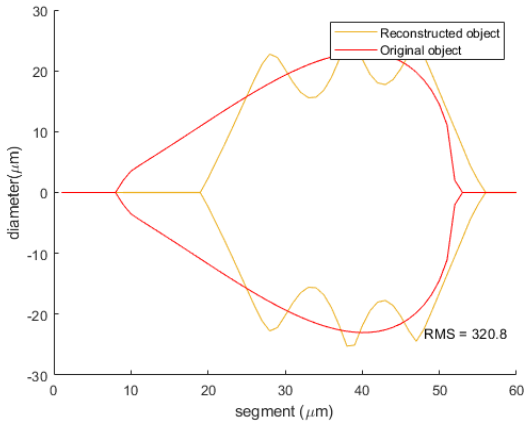

(c) Cost function correction and smoothing regularisation

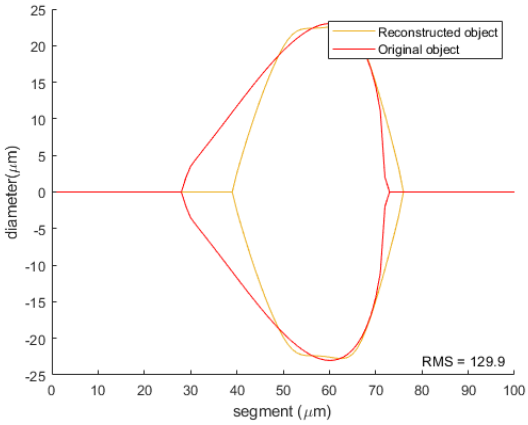

(d) Cost function correction, smoothing regularisation and resistance profile cropping

Fig. 5.11.: Reconstruction results from the simulated resistance profiles of the 44 μm teardrop particle. Addition of the correction steps occurs identically to figure 5.8

The reconstructions for the teardrop particle can be found in figure 5.11a up to figure 5.11d. Figure 5.11a shows the basic reconstruction. The shape is well traced, but once again there are large sidelobes. When the correction parameter is added in figure 5.11b, the result is once again very jagged, but notably when the same amount of regularisation is added as for the other objects in figure 5.11c, this jaggedness cannot be completely removed. When the resistance profile is cropped to the middle two thirds, where the resistance profile best matches the corrected model, the peaks are removed. The result only shows a small amount of the asymmetry which the original object has, but instead has the object moved off-centre on the x-axis.

5.2.3 Influence of assumptions in the model

The model does not take current inhomogeneity near the electrode-electrolyte interface into account. Instead, the earlier discussed liquid electrode setup is used and it is assumed that the current distribution is homogeneous at the measurement segment of the channel. The results for the liquid electrodes that were presented in [32] were verified using a simulation before using their liquid electrode setup in our experiments. Figure 5.12 shows how the vertical current distribution homogenizes along the length of the channel and becomes homogeneous after traveling a lateral distance equal to the height of the channel.

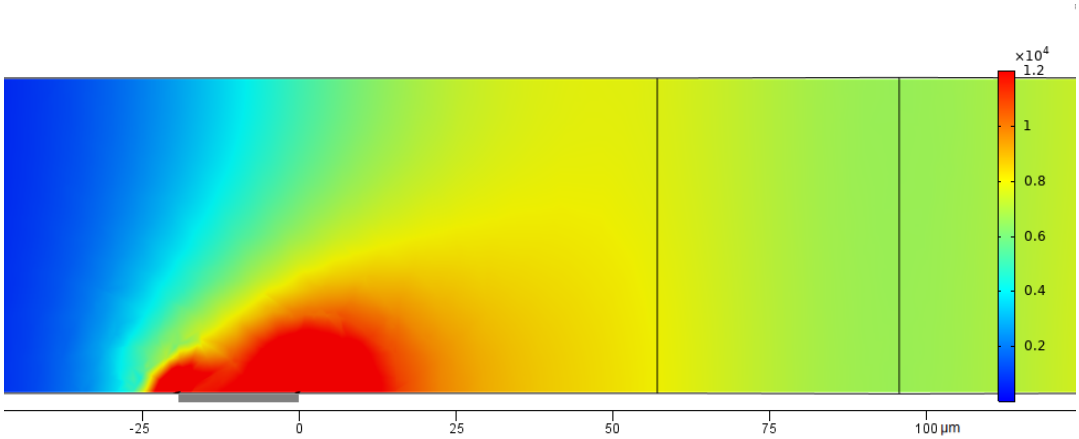

Fig. 5.12.: Current density distribution around one of the electrodes. Electrode is 20 μm long and highlighted with the gray bar. When looking at the current distribution at x=50 μm, it can be seen that the distribution is close to homogeneous. Vertical lines at x=55 μm and x=95 μm are the corners of the SRIM channel shape taper.

The COMSOL simulations were all run with empty space instead of a material for the object. To validate if this situation does not lead to large differences with the experimental values, several control simulations were run with polystyrene material objects in COMSOL, which has a specific resistance of 10^{14} Ωm. The differences in total current through the channel were below 0.001%.

To examine if disregarding the surrounding PDMS around the channel could have an influence on the simulated resistance profile, additional control simulations were run were the channel was surrounded by a block of PDMS. Only when the block size was significantly (10x) larger than the channel, a difference could be noted and this was most probably due to a changing mesh size. It was therefore assumed that the surrounding PDMS had a negligible effect on the resistance measurement.

5.3 Fabrication results

After fabrication of the master wafer, it was discovered that there was a small error in the mask design, due to which the triple inlet channels met each other at a slight offset, as shown in figure 5.13. This might have caused problems when flow focusing was implemented, but later results appear to show flow focusing working correctly on these chips. Furthermore, due to the lithography process, the corners on the chip are slightly rounded. However, as the SRIM channel itself does not contain important sharp corners, it is not expected that this will affect the measurement or the reconstruction to a great extent. The cracks visible in figure 5.13 are fixed when the SU-8 reflows slightly during the hardbake step.

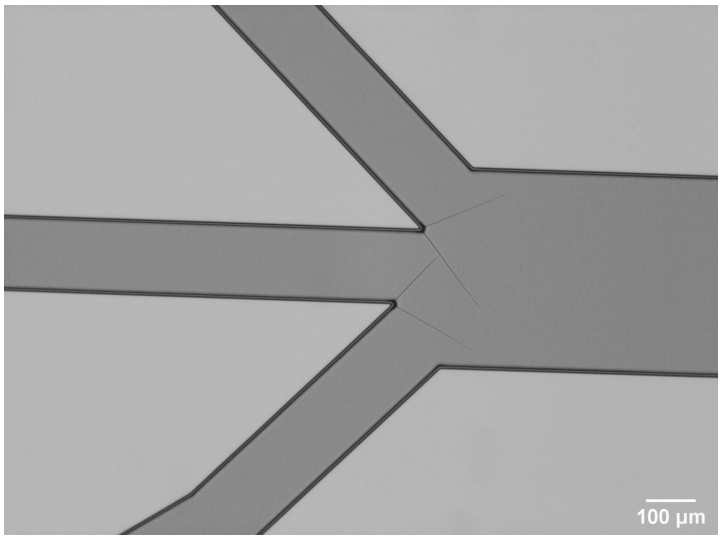

Fig. 5.13.: Offset in position flow focusing sidechannels.

Tab. 5.4.: Target and realized thicknesses of SU-8 layer of master wafers.

Target SU-8 layer thickness	Realized SU-8 layer thickness
50 μm	52 μm and 55 μm
10 μm	9.8 μm
8 μm	7.9 μm

The target thicknesses of the SU-8 layer were achieved within reasonable means as shown in table 5.4. During inspection of the 52 μm master, some height variation was detected, but this was all within 1 μm. The 30 μm custom particles were created successfully, as shown in figure 5.14. As the orientation of the particles could not be controlled after release from the wafer, it was difficult to characterise the particles accurately. The measurement of the particle thickness shown in the leftmost image of figure 5.14 shows a particle thickness of 26 μm, slightly below the intended size of 30 μm. Some height differences are expected as the height of the SU-8 layer on the wafer is not perfectly uniform either. From microscopic observations,

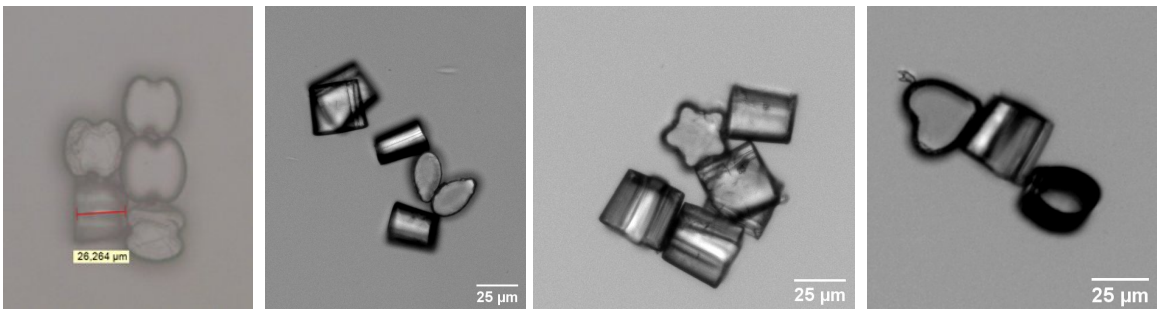

Fig. 5.14.: Custom SU-8 objects

the 2D shapes appear to have been replicated well from the lithography mask. Most of the smaller 6 μm custom particles were lost during retrieval from the solvent. Their small size made centrifugation to the bottom of the container tube more difficult and during the subsequent separation, they are suspected to still have been dispersed in the solvent.

5.4 Experimental results

5.4.1 Device characterisation

Figure 5.15a shows a Bode plot of the impedance and the phase response of the setup shown in figure 5.15b. Sweeps were conducted both with and without a bead present in the channel. The response with the incorporated bead is almost identical to the response without the bead.

The impedance shows a decreasing trend with increasing signal frequency with a plateau between approximately 10kHz and 500kHz. This impedance value at the plateau approximates the resistance calculated in the model. The frequency dependency of the phase change is different than expected from the ECM, although similar deviating phase response was also seen in earlier research [5]. The phase response reaches a local minimum of -9° at 100kHz.

Although this sweep was not conducted with the normal SRIM channel, but a section that lies besides it, it is expected that the insights about the frequency dependence of the impedance will be similar as if it was conducted with the SRIM channel, as the electrode-electrolyte interface is identical. However, the longer length of the channel should increase the value of the measured impedance and the increased distance between the sensing electrodes will decrease their capacitance. As it was harder to trap the bead in the SRIM channel, this longer section was chosen instead.

The occurrence of the impedance plateau around 100kHz and the minimal phase change at that frequency show that 100kHz is the best signal frequency to examine resistive effects on this

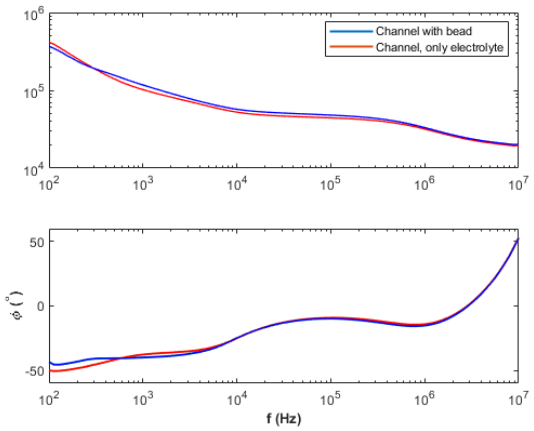

(a) Bode plot

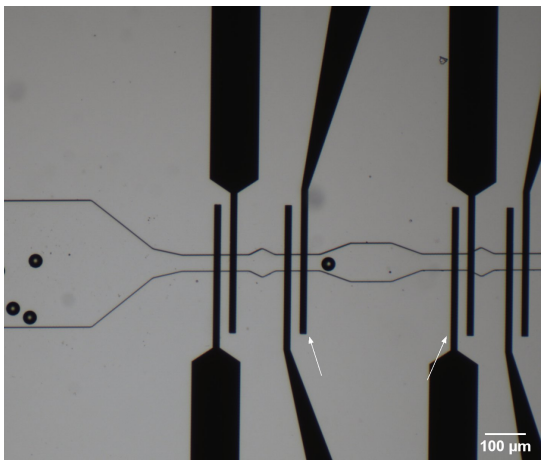

(b) Channel under investigation

Fig. 5.15.: (a) Bode plot of 50 μm SRIM channel on chip with and without 45 μm polystyrene bead. Differences in impedance and phase response are very small relative to the total values. (b) Image of the channel under investigation, with bead. The connected electrodes are marked with arrows.

chip. The -9° phase change indicates that non-resistive effects only account for 15.6%[3] of the impedance at this frequency meaning that any impedance changes measured at this frequency will mainly be caused by resistive effects.

5.4.2 Large beads

Figure 5.16 shows the passage of a 45 μm polystyrene bead through the 50 μm SRIM channel with figures 5.17a, 5.17b, 5.17c showing the corresponding impedance measurement and phase response. As the impedance increases as the bead enters the narrow SRIM passage, a corresponding phase response decrease can be seen, which after calculation shows that the impedance increase is 84% resistive. The signals of the beads are clearly distinguishable from the noise in the measurement.

[3] $Im(Z) = sin(\phi) \cdot |Z|$

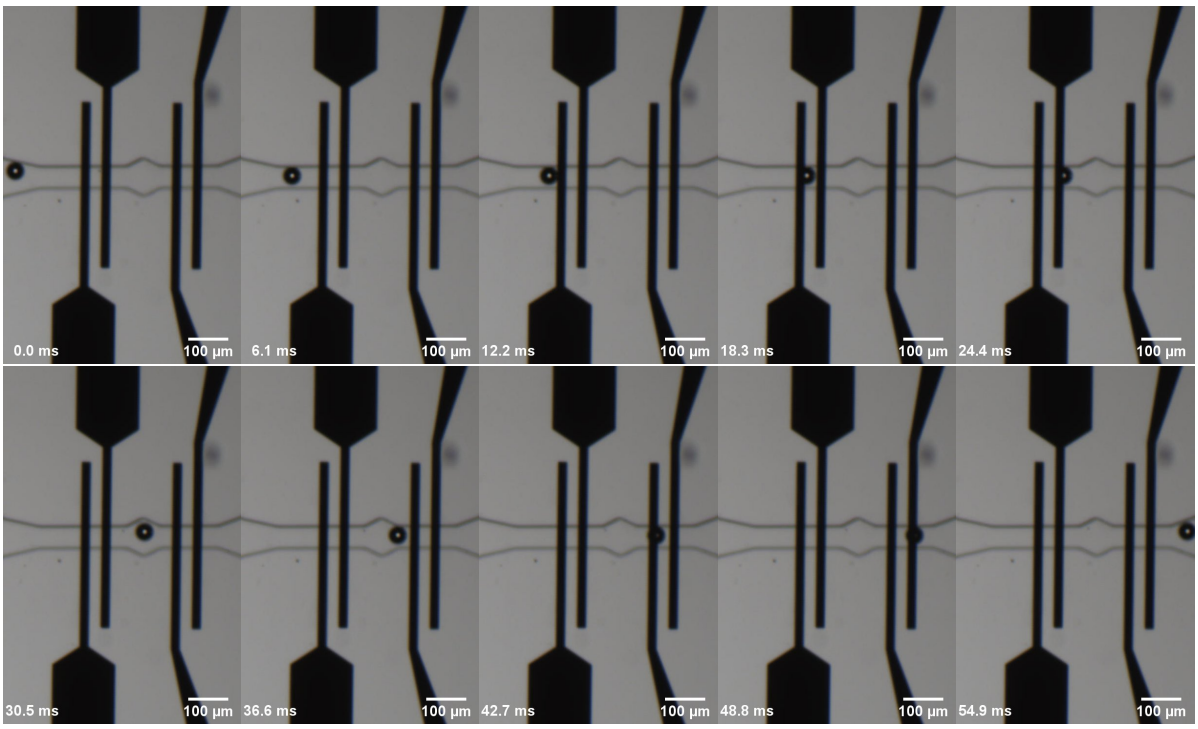

Fig. 5.16.: Video frames showing the passage of a bead through the SRIM channel. The inner two electrodes form the measuring pair.

Figure 5.17d shows the impedance measurement of the bead compared with values generated by the physics simulation and the SRIM model. The impedance values from the latter two were corrected to match the electrolyte conductivity used in the experiment. The measurement data shows a slight horizontal offset caused by an offset in the alignment of the chip with the electrodes during bonding. The profile was cut at the maximum values of the peaks seen in figure 5.17b. In figure 5.17d it can be seen that these maxima are located less than 120 μm apart. An explanation for this shorter distance is provided in section 6.4.

Figure 5.17e shows the same data, but for each impedance profile, the measured or simulated resistance value of the empty channel is subtracted. This step aims to remove any differences between the measurement and the other data caused by effects other than the passage of the bead. Although the values are relatively close for each set, both the absolute value as well as the swing amplitude still show differences in the order of 30%. This deviation might cause problems for the reconstruction of the object.

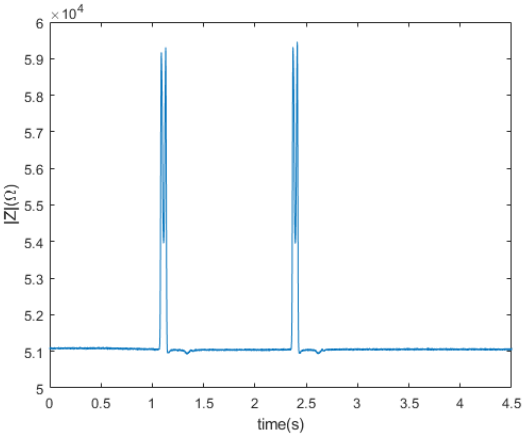

(a) Overview

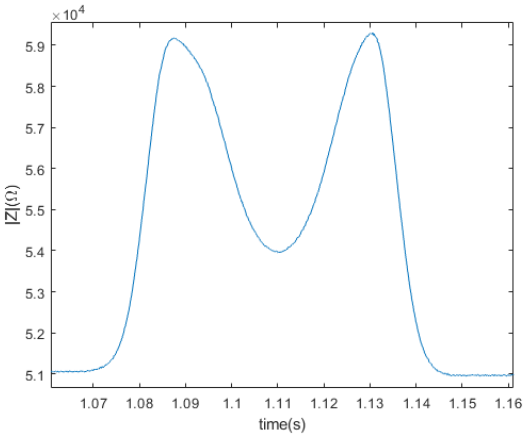

(b) Zoomed in

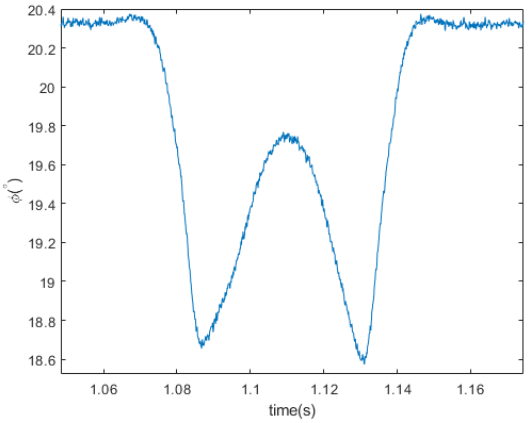

(c) Phase response

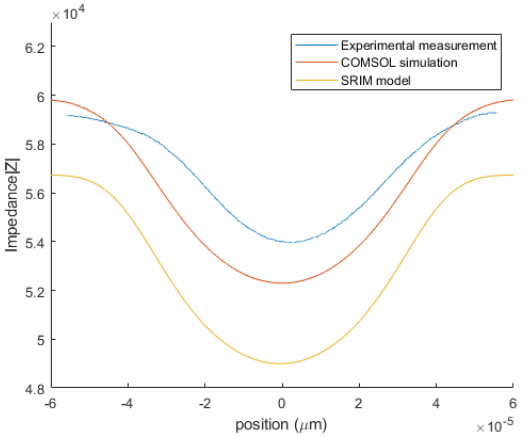

(d) Compared to simulation and model

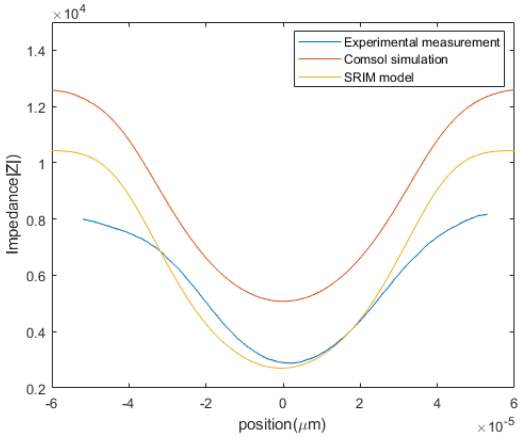

(e) Baseline value subtracted

Fig. 5.17.: 45μm beads passing through the SRIM channel. (b) zooms in on the signal of the first bead of (a). (d) compares the measured values with model and simulation results. (e) shows the same, but with the baseline value subtracted of the empty channel for the model, the simulations and the measurement results respectively.

5.4.3 Custom microparticles

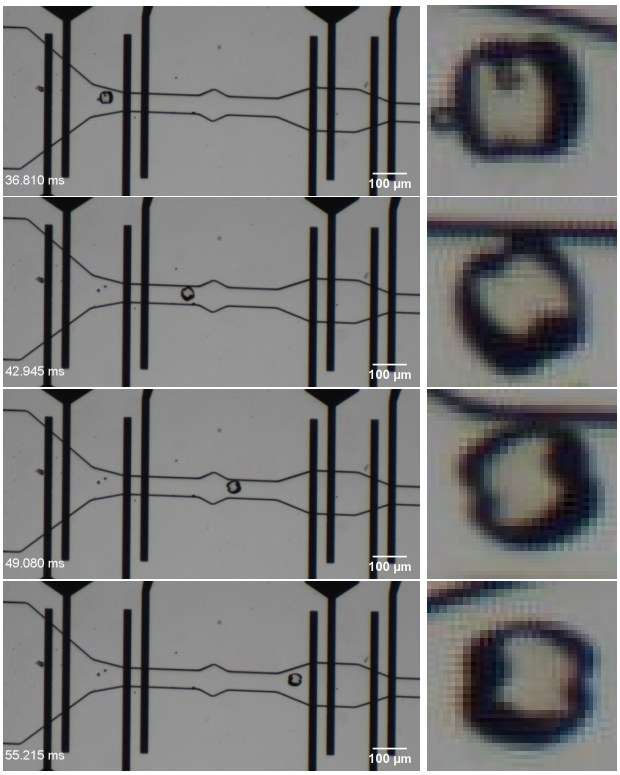

Fig. 5.18.: Video footage of fused ellipses particle traveling through SRIM channel. The closeups of the particle on the right clearly show the object rotation.

Figure 5.18 shows footage of a custom particle composed of fused ellipses traveling through the SRIM channel. The closeups on the right show how the particle rotates, although the frame rate is too low to determine the exact direction and rate of rotation. Figure 5.19a shows the impedance signal for the fused ellipse particle, a piece of SU-8 debris and a 45 μm bead from left to right. The signal of the custom particle and the debris are lower than the signal of the bead due to their smaller diameter. The signals of the bead and the piece of debris passed through the channel multiple times due to the required tapping against the tubing that was required to keep the custom objects moving.

As the distance between the sensing electrodes is much larger than for the 45 μm bead setup, the absolute value of this impedance signal is much higher. Figure 5.20 shows the measurement around the widest part of the channel compared to the model values. Because of the different channel length, the baseline value of the empty channel is subtracted from both results, just as with figure 5.17e. It can be seen that the width of the peak measured in the experiment is more narrow than for the model result. This might have to do with the irregular movement in combination with the translation from time labeled data to positional data. This is further discussed in section 6.4.

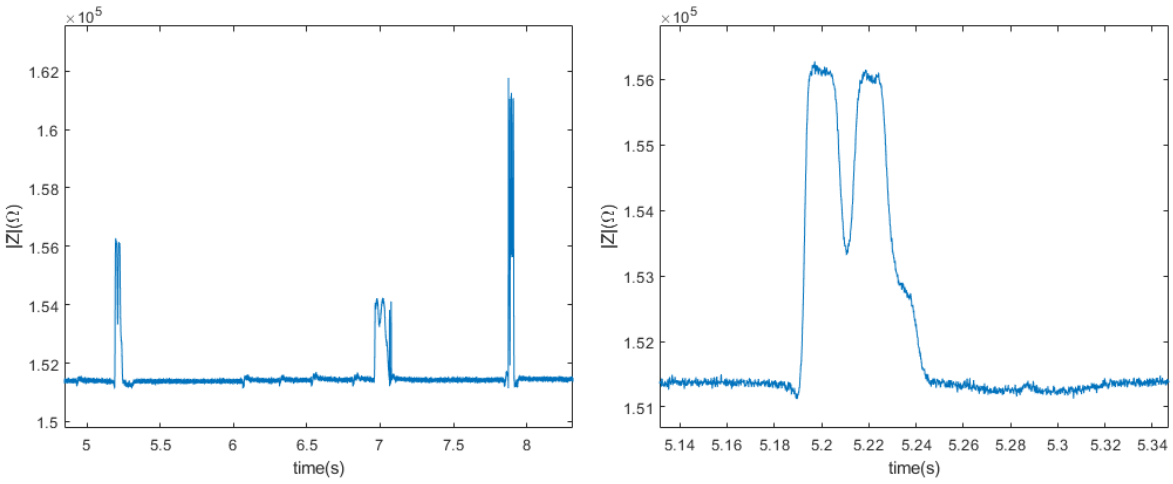

(a) Overview (b) Closeup

Fig. 5.19.: Impedance signal of the custom microparticle. (a) Overview of the impedance signals of respectively the custom object, some debris and a 45 μm bead, from left to right. (b) shows a closeup of the custom microparticle.

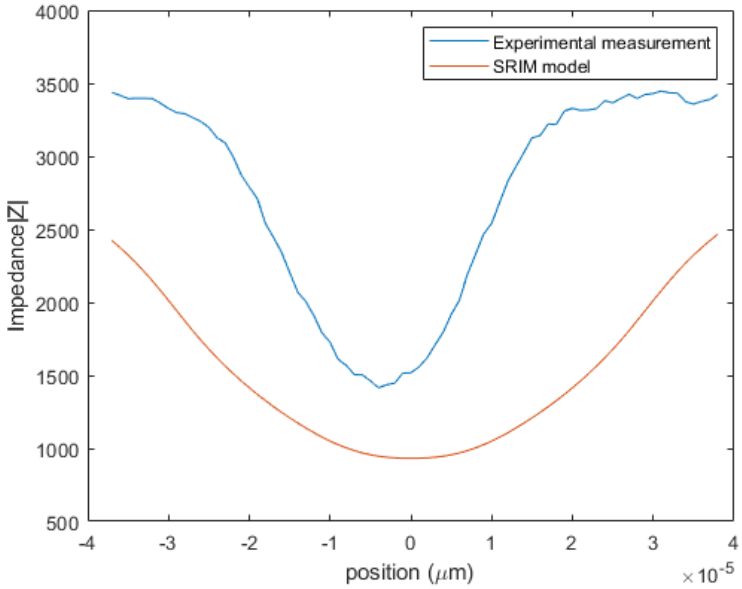

Fig. 5.20.: Custom microparticle measurement compared to model result. The empty channel baseline value is subtracted from each impedance profile respectively.

Two solutions were examined to reduce the amount of shear force that the particle experiences in the SRIM channel and the resulting rotation. The first is hydrodynamic flow focusing, shown in figure A.1 in the appendix, which means to center the particle. This however did not reduce the amount of rotation noticeably. The second solution was to increase the density of the electrolyte by increasing the NaCl mass concentration to 21.9%. This reduced the amount of rotation somewhat, but did not completely remove it. Additionally, the resulting smaller density difference between the particles and the electrolyte caused the particle to pass through the channel more easily, presumably because it was stuck to the bottom less often. This also reduced the irregularity of the movement speed.

5.4.4 8 and 10 um channels

Due to clogging and bonding issues, we ran into a shortage of of the smaller sized chips at the end of the experimental phase. Experiments where sperm and small beads were measured, were performed on a 7.7 μm high and 10 μm wide channel. If the smaller 8 μm wide channel would still have been available, it would have resulted in a higher signal to noise ratio.

Figure 5.21 shows the passage of a sperm cell through the SRIM channel. The sensing electrodes are the electrodes closest to the channel and are space 50 μm apart. Figure 5.22 shows six impedance measurements of sperm cells passing through the SRIM channel. Although the fluid flow speed should be stable, there is an almost 200% variation in the passing time of the sperm. The height of the peaks appears consistent among the measurements. The amplitude of the noise is approaching the amplitude of the signal, with a signal to noise ratio of 6.1. Notable is that each of the signals is asymmetrical, with the larger peak occurring later. However, later measurements with beads on the same chip (figures 5.23e and 5.23f show the same asymmetry. Thus, it is more probable that this asymmetry is caused by the offset alignment of the electrodes, as shown in figure 5.21, then by the sperm shape or the presence of the sperm tail.

Figures 5.23a and 5.23b show measurements of sperm cells mixed with 5 μm beads. The impedance signals of the beads have a SNR of 18.4, approximately 3 times higher than the sperm cells. The impedance signal shows smaller bumps to the side of the main peaks.[4] The reversed asymmetry of the signals in figures 5.23a to 5.23f compared to figure 5.22 is caused by reversed flow.

[4]These bumps to the side of the main peak are probably caused by the influence of the bead on the electric field in the channel, while the bead is still outside the actual measurement channel. The decrease in impedance as the bead is closer to the electrode is presumably due to a specific distance between the bead and the electrode where the current is able to 'wrap around' the bead, which leads to reduced resistance.

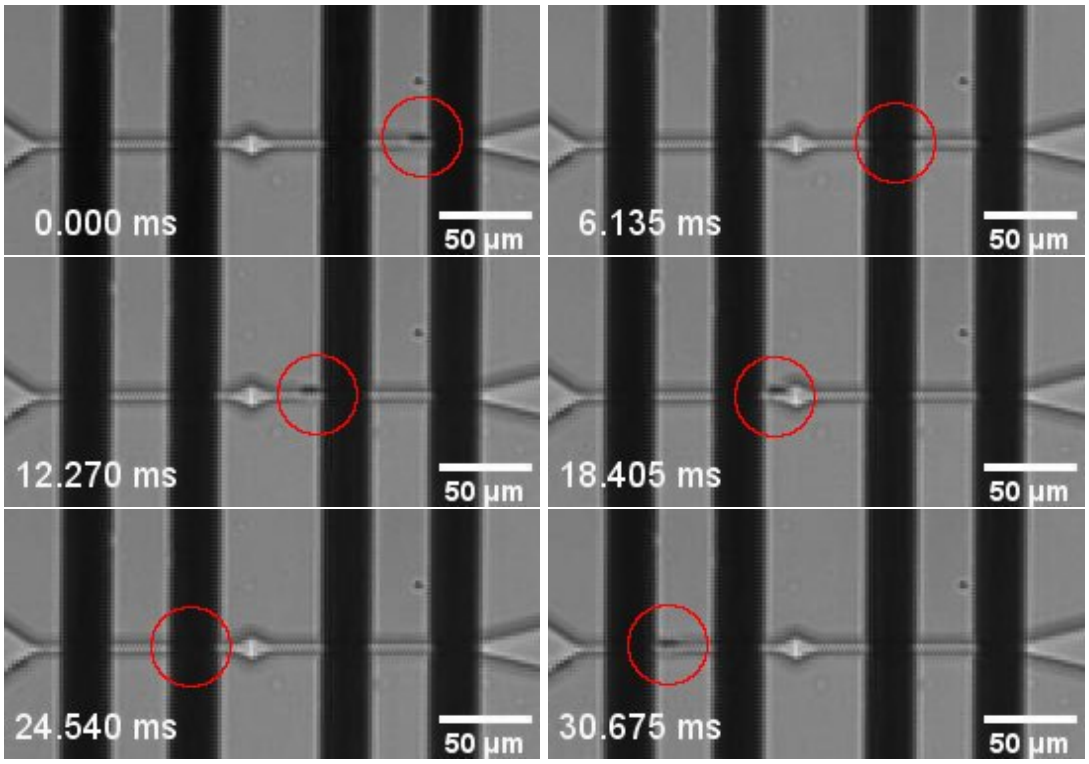

Fig. 5.21.: Video footage of sperm cell traveling through SRIM channel.Sperm location is accentuated with red circle.

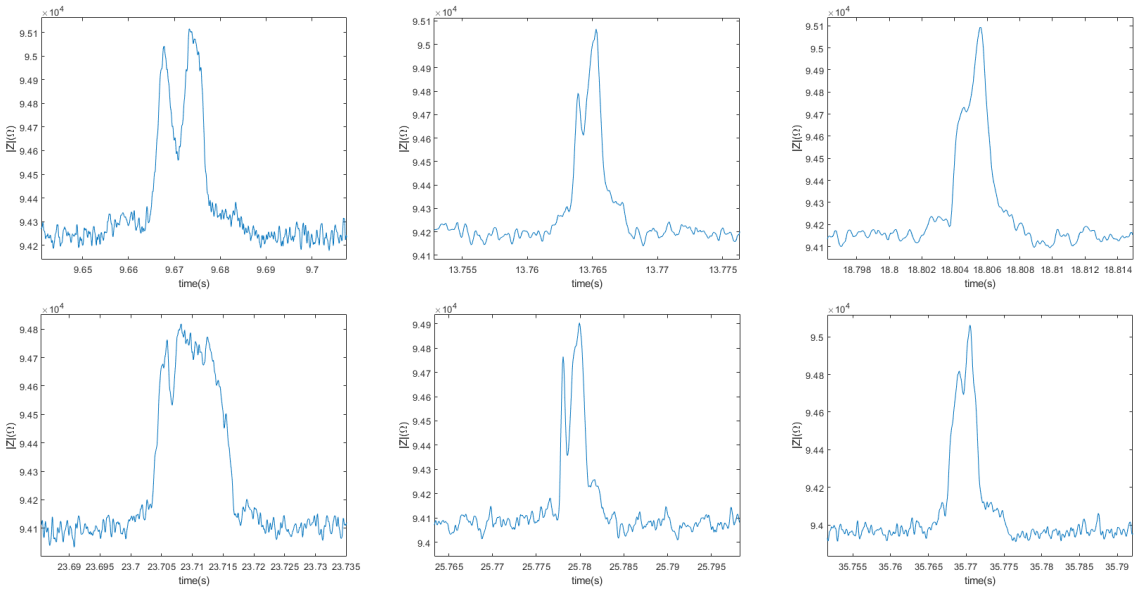

Fig. 5.22.: Impedance measurements of sperm cells. Note that the timescale may differ up to a factor 2.

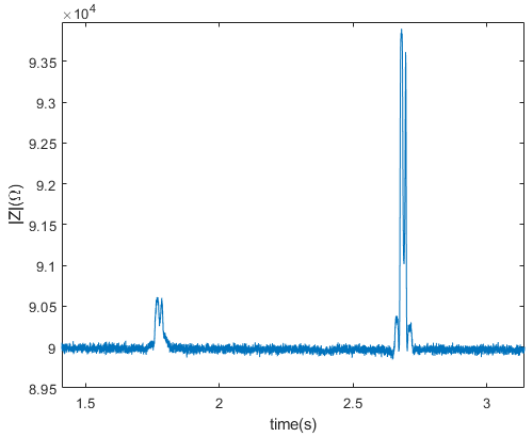

(a) Overview of passing sperm and bead respectively

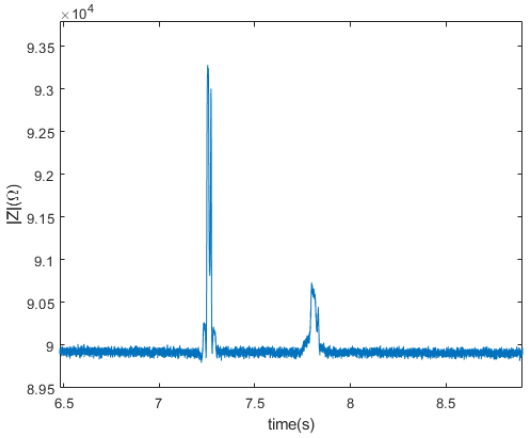

(b) Overview of another pair of passing bead and sperm

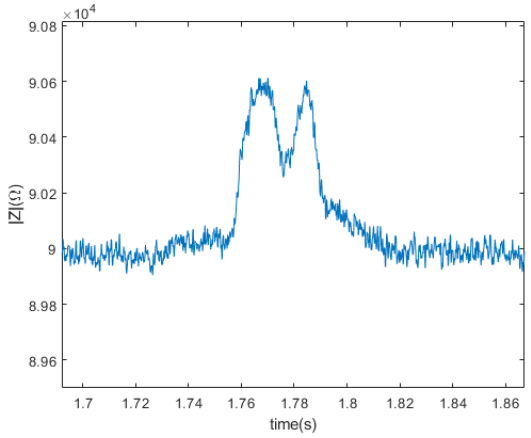

(c) Closeup of the first sperm cell

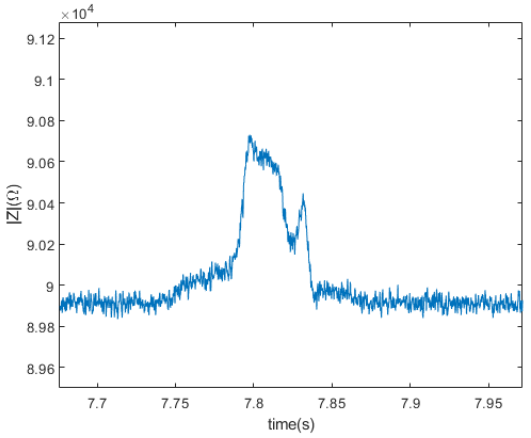

(d) Closeup of the second sperm cell

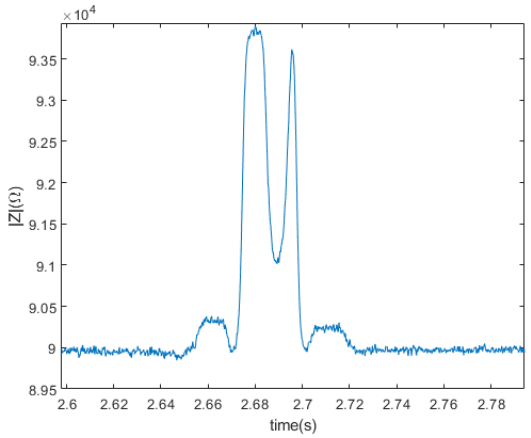

(e) Closeup of the first 5 μm bead

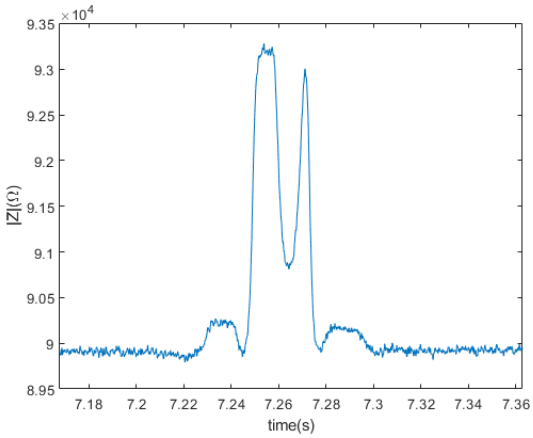

(f) Closeup of the second 5 μm bead

Fig. 5.23.: Impedance signals of sperm cells and 5 μm beads.

5.4.5 Reconstruction results

Figure 5.24 shows the SRIM reconstruction from the impedance measurement of a 45 μm bead. Before reconstruction, a baseline correction as seen in figure 5.17e was performed. Furthermore regularization with the same settings as in section 5.2.1 was applied, but no profile cropping. The reconstruction approximates the bead in size, with the result being within 20% of both the length and the width of the original bead. The shape of the reconstruction differs substantially however, with the reconstructed shape having two wide appendages at its ends.

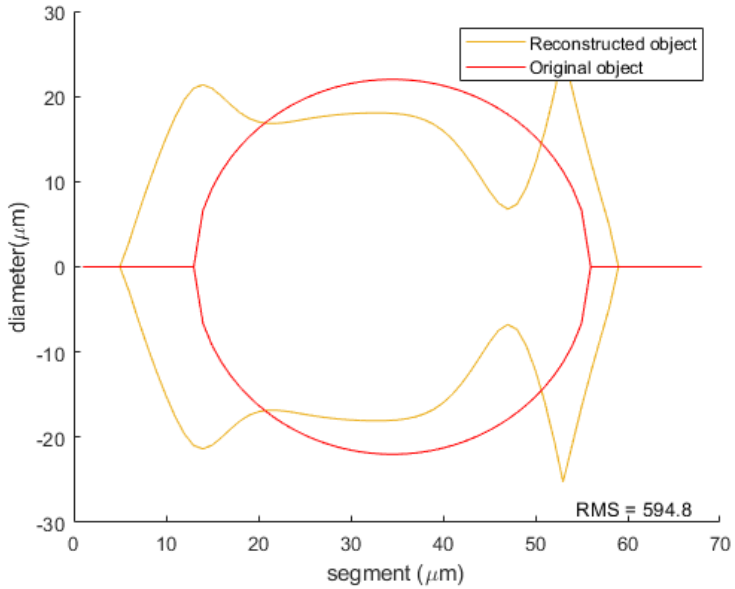

Fig. 5.24.: SRIM reconstruction from measured impedance of 45 μm bead.

Figure 5.25 shows the reconstruction result from the impedance measurement of the custom microparticle shown in figure 5.19b. Two large peaks can be seen at the sides of the location where the particle is supposed to be, with some very small peaks in between. The erroneous translation from the time-labeled data due to irregular particle movement in combination with the rotation of the particle, make it very hard to perform an accurate shape reconstruction.

Reconstructions of the 6 μm beads and the sperm cells were not attempted. The impedance signals of the small beads and the sperm cells had too much noise to attempt a reconstruction.

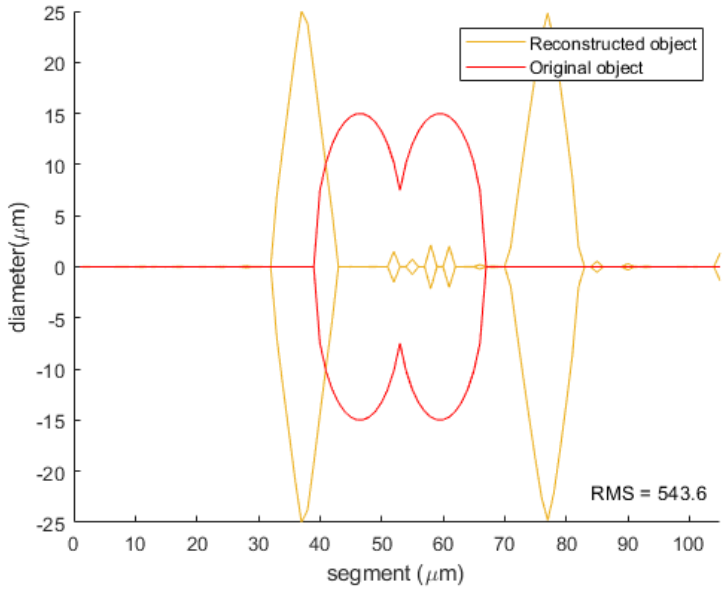

Fig. 5.25.: SRIM reconstruction from measured impedance of custom microparticle.

5.5 Classification experiment

In the classification experiment, model resistance profiles of objects were compared with the COMSOL simulation values to decide which object shape provided the best fitting result. This was done by calculating the cost function that is also used in the optimization. Here, the cost function calculates the summed square of the deviation between the model resistance profiles of the three provided objects and the given COMSOL resistance profile. Additionally, positional offsets were added to the object in the COMSOL simulations to provide variation in the signal and check for robustness of the classification.

Table 5.5 shows which COMSOL resistance profiles and for which positional offsets, the classification was able to successfully determine which object corresponded to it. Table A.1 in the appendix includes the cost function scores for each object. Positive front/back offsets indicate a forwards offset, while negative values indicate a backward offset relative to the movement direction. The classifications for no offset and the offsets of 1 μm forwards and backwards were determined correctly for all particles. The offset positions where the sphere was set more than 5 μm forward resulted in classifications of the sphere as a teardrop particle and vice versa when the teardrop particle was moved backward. This seems to be due to the asymmetry of the teardrop particle, which gives a similar cost value change as these positional offsets.

The 0 to 1.5 μm positional difference in height had only a very minor effect on the value of the resistance signal, with a maximum of 0.19% change of the signal. The classification results for

Tab. 5.5.: Classification results for the different shapes and resistance profile variations.

Shape	Sphere										
Height offset (μm)	0	0	0	0	0	0	0	0	0	0	0
Front/back offset (μm)	-15	-10	-5	-3	-1	-0	1	3	5	10	15
Correctly classified	y	y	y	y	y	y	y	y	n	n	n

Shape	Fused ellipsoids										
Height offset (μm)	0	0	0	0	0	0	0	0	0	0	0
Front/back offset (μm)	-15	-10	-5	-3	-1	-0	1	3	5	10	15
Correctly classified	n	y	y	y	y	y	y	n	n	n	n

Shape	Teardrop										
Height offset (μm)	0	0	0	0	0	0	0	0	0	0	0
Front/back offset (μm)	-15	-10	-5	-3	-1	-0	1	3	5	10	15
Correctly classified	n	n	n	y	y	y	y	y	y	y	y

these signals, which were all correctly classified, are therefore omitted, as they gave a distorted overview of the classification capabilities.

6 Discussion

This chapter discusses the quality of the results presented in the previous chapter and places these results into their context within this research. Furthermore it goes into several of the main hurdles in this research.

6.1 Reconstruction and classification performance

Shape reconstruction results from COMSOL physics simulation data show very promising performance in the identification of object shape. Even when no corrections are applied to the basic resistive model, the reconstruction method is able to fairly accurately determine overall object shape as shown in figures 5.8a, 5.10a and 5.11a. These reconstructions have very large sidelobes however, which are probably artifacts caused by compensation for current inhomogeneity, since the model does not take this into account and therefore produces a lower resistance value than the physics simulation.

Corrections in the model allow for removal of these sidelobes and better detail resolution, but as shown by the worsened reconstruction of the teardrop object in figure 5.11d, some adjustment of the settings is still required to find a middle ground which allows for adequate resolution of all relevant features.

The reconstruction from the measurement data of the 45 μm bead was able to size both the length and the width within 20% of the size of the particle. The reconstruction also showed sizable sidelobes, which might be caused by the earlier mentioned reasons. Further examination of the measurement setup and the underlying current flow might lead to improvements of the model and the resulting reconstruction.

The fitting of the model corrections can be tuned for the differentiation of any morphological feature set. Overfitting of these corrections towards a perfect reconstruction result is a risk, but this can be circumvented by training the method as a classification method, where the correction factors have to be flexible towards different shapes.

The results of the classification experiment showed how the SRIM model is able to distinguish a sphere from a particle with a ridge for very small offsets (up to 2% of the object size) of the expected position of the object. The classification experiment mistook further offsets for

asymmetry of the object. The performance of the classification could be improved with the same model improvements that would lead to better shape reconstructions, discussed in the next section.

When comparing the capabilities of SRIM with existing technologies, it must be noted that existing technologies like RPS are well-established and have reached beyond the sizing of microscale object. RPS was recently shown to be able to measure nanoparticles within 6% of their size.[38] It can simply be said that SRIM in its current form is not able to approach this. However, SRIM offers a new method for object shape analysis from impedance measurements, for which there is little literature to compare its performance. Shaker et al presented a method for morphology analysis of budding yeast cells, but this was limited to the length to width ratio [32].Different methods for this were proposed by Qiu et al (2015) [39] and Pevarnik et al (2012) [40], but SRIM would in theory be able to resolve the shape further than the aforementioned works, as they were mostly limited to distinguishing the length of their objects.

6.2 Resistance model correction

As seen in tables 5.2 and 5.3 in the results, which show the resistance values of suspended spheres of different sizes, the resistance model used in SRIM deviates most as the cross sectional width of the object decreases relative to the channel cross section. This means that the SRIM model will have decreased performance for small objects or objects which have thin segments.

The relationship between the measured resistance in resistive pulse sensing and the size of the embedded object has been the subject of multiple investigations, whose results are used to this day in cell sizing. Unfortunately, the most commonly used equations are based on the base equation of Maxwell's mixing theorem as discussed in chapter 3.2. This makes these corrections inapplicable to our implementation of resistive pulse sensing. To improve performance of our method however, the most beneficial task would be to improve the resistance model.

Interestingly, when SRIM compensates for the lower model resistance prediction, it does this by adding sidelobes, instead of increasing the object size. When looking at current density maps of the COMSOL simulations, like figure 5.9, it can be seen that low current density areas occur at the same location as these sidelobes, albeit with a different shape. This phenomenon could be useful in further correction of the model.

6.3 Particle rotation

One significant problem encountered in the experiments was the tumbling movement of non-spherical particles. This was most probably caused by shear forces due to the parabolic flow velocity profile. It must be noted that the spherical beads could also have rotated, but this had no effect on their impedance measurement due to their rotational symmetry. This tumbling movement makes it impossible to perform SRIM on these non-spherical particles.

If the rotation of the object would be known exactly, this could be incorporated in the model, but unfortunately the movement cause by the shear forces is very dependent on small changes in object shape and position and therefore highly unpredictable. Furthermore Qiu et al [39] reported that rotating objects may displace an effective volume greater than their geometrical volume, which could also influence measurements.

The efforts undertaken in the experiment, slightly improved this issue, but failed to remove the rotation enough for successful SRIM. Earlier research however was successful in stabilizing asymmetrical particles to examine their dimensions using DEP alignment [32], which might provide similar beneficial effects in SRIM.

6.4 Practical problems

Sampling rate

Due to a miscalculation, the sampling rate of 2kHz was set lower then what would be ideal for the SRIM datacollection, due to which some interpolation had to be applied to have a datapoint at every 1 μm of movement. As the Zurich HF2LI has capacity for much faster sampling, only at the cost of increased data size, it would be recommended to carry out further examinations at a higher sampling frequency. 20kHz should be fast enough to capture all relevant data at the flow speeds used in this work. The sampling rate was kept during the experiments of this research, because at higher sampling frequencies with corresponding higher lowpass filter frequency, the output driving signal frequency became visible in the input. This obscured the impedance signal of the passing objects and was deemed to cause too many complications in the data analysis.

Framerate-data discrepancy

A discrepancy can be found between the footage and the measurement in the time that the bead takes to travel through the measurement path. The footage shows a duration of approximately

20ms while the measurements show 43ms between the tips of the impedance peaks. It is suspected that this is caused by a processing error of the video footage, the timing of the impedance data corresponds with velocity calculations based on the flow speed and the channel width. Furthermore, other difficulties have been encountered with the camera setup as well.

Time-position translation

The experimentally measured resistance profile of the 45 μm bead was cut at the maximum values of the peaks seen in figure 5.17b. In figure 5.17d it can be seen that the maxima are located less than 120 μm apart, meaning that either these maxima are found at some distance from the electrode, or the script that translates the time labels of the data to positions has a slight error. The second is likely, as the current translation method is bases the object velocity at the widest part of the channel on the total flow speed provided by the syringe pump. Due to the non-uniform flow profile, there will be a difference between this average fluid velocity and the actual object velocity. Furthermore, in the measurements of the custom microparticle, the movement speed was very irregular, which causes the translation from time to position to differ quite significantly. This could explain the smaller width of the blue peak in figure 5.20 compared to the model result. This would also affect the shape of the reconstruction.

Noise level

Quantification of the noise lead to a noise level that was 1000x higher than what was expected for pure thermal noise, calculated with the Norton equivalent of the equation for the Johnson-Nyquist noise which gives the root mean square value of the noise current:

$$i_n = \sqrt{\frac{4k_bT\delta f}{R}} \tag{6.1}$$

It is unclear what the reason for this is or which other source of noise could cause this much higher level of noise. It is suspected that a calculation error might be the cause of the discrepancy. To confirm if the noise has a thermal origin, noise measurements could be performed at different temperatures. By measuring at various temperatures between 0°C and 100°C, a notable difference of around 30% should be found if the main source of the noise is thermal. As the measurements of the sperm cells and the small beads are limited by the noise level, it is important to reduce this noise.

Chip issues

The microfluidic chips were prone to clogging when the flow speed was increased. Unfortunately, this is a common problem encountered in microfluidics. The mechanisms through which this occurs and the designs various features which prevent this are an ongoing field of research.[41][42]

The bonding protocol for these chips should still be refined further. At increasing plasma activation times, the bonding strength increases to such a strength that a small layer of PDMS remains attached to the glass after removal of the chip. This residue may interfere with further bonding and possible cause blockage of the channels when a new chip is bonded to the glass. Especially for the chips containing the smaller channels, the possibly uneven layer of PDMS may cause problems. Although a solvent, Polygone, can be used to remove the residue, it is difficult to verify whether this completely removes all residue and leaves the rest of the chip unaffected.

Alignment of the electrodes and the channels proved to be a difficulty. As the microscope setup for the alignment tool was slightly out of plane compared to the vertical movement of the XYZ stage of the alignment tool, the PDMS chip part appeared to move slightly in the horizontal plane relative to the electrodes. Furthermore, it is sometimes unclear what height difference still remains when lowering the PDMS. With practice, it should be possible to compensate for this, but in the experiments in this work, some offset remained in the chips. This offset should be compensated for in the SRIM model or the result will also be offset. If the offset of the alignment is large enough that the broadening sector is too close to the electrodes for the electric field to homogenize, it could also influence the measurement results.

7 Recommendations

The recommendations for further research can be divided in three main directions: examination of the effect of channel shape on the effectiveness of SRIM, improvement of the SRIM impedance model and improvements in the experimental setup.

7.1 Channel shape

The channel through which the investigated object travels during SRIM needs to balance two factors: on the one hand SRIM requires channels of varying width to build its set of resistance equations, but on the other hand, these variation in width should not be too large, as the resistance model will have to compensate for the resulting increased current inhomogeneity. Different channel designs than the ones that are currently used could however have improved performance in resolving specific object shapes. The examination of the effect of channel design on SRIM effectiveness could therefore provide interesting results.

7.2 Model improvement

Comparisons of the resistance profiles generated in the model, COMSOL physics simulation and in the experiments show sizable differences. Expansion of the resistance model to compensate for the curvature of current around the examined object could therefore lead to major improvements in SRIM results. The difficulty herein is that the resistance model cannot be reinvented completely as the shape reconstruction principle relies on a method which calculates the shape of the object with cross sectional segment widths. The addition of non-resistive impedance effects into the model could also lead to lower error of the model, as approximately 16% of the impedance now goes unexplained by only taking into account resistance.

One of the simpler implementable corrections would be the path correction proposed by Romano et al. [43]. This article proposed to approach the path of the current as a cone originating from the apex formed by the slope of the walls instead of orthogonal to the cross sections done in our model. Further improvements can also be found in the field of thermodynamics. Although this field describes a different phenomenon, parallels can be drawn, with the analogies of heat flow

for electrical current, temperature for electrical potential and thermal resistance for electrical resistance. Furthermore, geometries similar to the geometry used in SRIM have more often been examined in thermodynamics, in for example heat exchange systems.

The weights of the correction factors require tuning for optimal results from the SRIM method for both classification and general shape analysis applications. Care should be taken that improved performance towards the recognition of one shape characteristic does not lead to reduced performance for other characteristics. Machine learning methods, which often work by tuning certain parameters in their algorithms to suit their training data, could help with the adjustment of the correction factors.

7.3 Improvements in experimental setup

Finally, there are several improvements in the experimental method that could lead to new and improved results.

Differential measurement should be kept in mind if new electrodes are fabricated. Because of the usage of the existing electrode layout, differential measurement was not possible in this research as identical electrical paths could not be created without interference of floating electrodes. Differential measurement however remains an excellent method of common mode noise repression. Increasing the signal to noise ratio in this way might enable the usage of SRIM on sperm cells. Flow focusing with non-conducting sheath flows could lead to further improvements of the SNR for small object.

Tracking of object passage with high-speed cameras could help with improving the time-to-position translation, as currently the camera footage was unsuited to verify its performance.

The method of aligning object using dielectrophoresis discussed in earlier research [32] and mentioned in the discussion could stabilize objects for SRIM examination. DEP manipulation of sperm cells has been performed earlier in our group. [5]

8 Conclusion

This work presents a method of determining object shape through the usage of computational optimization from impedance measurement using coplanar electrodes in a microfluidic channel. Although the concept of using the channel geometry together with the impedance changes measured during the passage of an object to determine the object shape is not totally new [9][39][40], SRIM is the first method which in theory is able to completely resolve the shape.

The original aim of this research was to find a method for the identification of motility and morphology characteristics of spermatozoa. Although motility was not further examined, in theory SRIM is a suitable method to examine sperm morphology. Objects with shapes characteristics that can be encountered in (abnormal) sperm morphology, like ridges, curves and head/tail bulging, were passed through a SRIM channel in COMSOL physics simulations and the resulting resistance simulation data could be used to extract the shape of the used object.

To improve the practical viability of SRIM for sperm morphology examination, the signal-to-noise ratio of the measurement should be improved as the cell's small size relative to the channel dimensions causes difficulty in acquiring a clean signal. Furthermore, either the model's performance for small objects should be improved or the size of the conducting channel for example be reduced with a nonconducting sheath flow. Further improvements for the general applicability of the SRIM method lie in the expansion of its impedance model, the examination of the effect of channel shapes on reconstruction quality and increased control over the orientation of non-spherical objects. Furthermore, adjustment of the correction factors in the model can optimize the accuracy of the model. Machine learning methods can aid in this adjustment, as they specialize in the search for fitting parameters that suit their training data.

The measuring setup for SRIM is relatively simple in its construction, although its usage is subject to common problems encountered in microfluidics like clogging. As a simple platform, it can however also benefit from the many improvements that are invented for these issues. Simulation performance of SRIM led to promising results and experimental results show first signs of the technique being a viable option for shape analysis of microparticles, although much has to be improved in the practical approach before more concrete results can be gathered. Non-optical morphology analysis of cells is a relatively unexplored subject, but can provide its uses in for example sperm quality analysis. With this work we hope to provide a new approach in this field.

Bibliography

[1] Milad Manafi, ed. *Artificial Insemination in Farm Animals*. en. InTech, June 2011 (cit. on p. 1).

[2] World Health Organization, ed. *WHO laboratory manual for the examination and processing of human semen*. 5th ed. OCLC: ocn646393549. Geneva: World Health Organization, 2010 (cit. on p. 1).

[3] Roelof Menkveld, Cas A.G. Holleboom, and Johann P.T. Rhemrev. "Measurement and significance of sperm morphology". In: *Asian Journal of Andrology* 13 (1 Jan. 2011), pp. 59–68 (cit. on pp. 1, 2).

[4] Jm Morrell. "Update on Semen Technologies for Animal Breeding*". en. In: *Reproduction in Domestic Animals* 41.1 (Feb. 2006), pp. 63–67 (cit. on p. 1).

[5] B. de Wagenaar, S. Dekker, H. L. de Boer, et al. "Towards microfluidic sperm refinement: impedance-based analysis and sorting of sperm cells". en. In: *Lab on a Chip* 16.8 (2016), pp. 1514–1522 (cit. on pp. 1, 3, 15, 28, 44, 62).

[6] Sholom Shuchat, Sinwook Park, Shahar Kol, and Gilad Yossifon. "Distinct and independent dielectrophoretic behavior of the head and tail of sperm and its potential for the safe sorting and isolation of rare spermatozoa". en. In: *ELECTROPHORESIS* 40.11 (June 2019), pp. 1606–1614 (cit. on p. 1).

[7] Johanna T. W. Berendsen, Jan C. T. Eijkel, Alex M. Wetzels, and Loes I. Segerink. "Separation of spermatozoa from erythrocytes using their tumbling mechanism in a pinch flow fractionation device". en. In: *Microsystems & Nanoengineering* 5.1 (Dec. 2019), p. 24 (cit. on p. 1).

[8] Neil Convery and Nikolaj Gadegaard. "30 years of microfluidics". en. In: *Micro and Nano Engineering* 2 (Mar. 2019), pp. 76–91 (cit. on p. 2).

[9] Vasileios Papadimitriou. "Ion concentration polarization: focusing, separation, extraction and particle porosity differentiation". PhD. Enschede, The Netherlands: University of Twente, Oct. 2019 (cit. on pp. 2, 63).

[10] Makusu Tsutsui, Takeshi Yoshida, Kazumichi Yokota, et al. "Discriminating single-bacterial shape using low-aspect-ratio pores". In: *Scientific Reports* 7 (1 Dec. 2017), pp. 1–9 (cit. on p. 5).

[11] R. Maugi, P. Hauer, J. Bowen, et al. "A methodology for characterising nanoparticle size and shape using nanopores". In: *Nanoscale* 12 (1 Jan. 2020), pp. 262–270 (cit. on p. 5).

[12] Tanja Hamacher, Johanna T. W. Berendsen, Stella A. Kruit, Marleen L. W. J. Broekhuijse, and Loes I. Segerink. "Effect of microfluidic processing on the viability of boar and bull spermatozoa". en. In: *Biomicrofluidics* 14.4 (July 2020), p. 044111 (cit. on p. 7).

[13] Sami Franssila. *Introduction to microfabrication*. 2nd ed. Chichester, West Sussex [England]: John Wiley & Sons, 2010 (cit. on pp. 8, 9).

[14] Angel Flores and Michael R. "Soft Lithographic Fabrication of Micro Optic and Guided Wave Devices". en. In: *Lithography*. Ed. by Michael Wang. InTech, Feb. 2010 (cit. on p. 8).

[15]Y. Xia and G. M. Whitesides. “Soft Lithography”. In: *Annual Review of Materials Science* 28 (1998). 604, pp. 153–184 (cit. on p. 8).

[16]A. R. Vollertsen, D. de Boer, S. Dekker, et al. “Modular operation of microfluidic chips for highly parallelized cell culture and liquid dosing via a fluidic circuit board”. en. In: *Microsystems & Nanoengineering* 6.1 (Dec. 2020), p. 107 (cit. on p. 9).

[17]Mark A Eddings, Michael A Johnson, and Bruce K Gale. “Determining the optimal PDMS–PDMS bonding technique for microfluidic devices”. In: *Journal of Micromechanics and Microengineering* 18.6 (June 2008), p. 067001 (cit. on p. 9).

[18]BIOS Lab-on-a-chip group. *Tutorial reader Lab-on-a-chip course*. University of Twente (cit. on p. 9).

[19]Kwang W. Oh, Kangsun Lee, Byungwook Ahn, and Edward P. Furlani. “Design of pressure-driven microfluidic networks using electric circuit analogy”. en. In: *Lab Chip* 12.3 (2012), pp. 515–545 (cit. on p. 10).

[20]Yu-Jui Chiu, Sung Hwan Cho, Zhe Mei, et al. “Universally applicable three-dimensional hydrodynamic microfluidic flow focusing”. en. In: *Lab on a Chip* 13.9 (2013), p. 1803 (cit. on p. 10).

[21]W Olthuis. “Measurement science for engineers”. In: ed. by P. P. L. Regtien. London ; Sterling, VA: Kogan Page Science, 2004 (cit. on pp. 10, 11).

[22]R. W. DeBlois and C. P. Bean. “Counting and sizing of submicron particles by the resistive pulse technique”. In: *Review of Scientific Instruments* 41 (7 July 1970), pp. 909–916 (cit. on pp. 12, 13, 32).

[23]James Clerk Maxwell. *A Treatise on Electricity and Magnetism*. Cambridge: Cambridge University Press, 2010 (cit. on p. 12).

[24]I. Sevostianov, S.G. Mogilevskaya, and V.I. Kushch. “Maxwell’s methodology of estimating effective properties: Alive and well”. en. In: *International Journal of Engineering Science* 140 (July 2019), pp. 35–88 (cit. on p. 12).

[25]W. R. Smythe. “Flow around a spheroid in a circular tube”. In: *Physics of Fluids* 7 (5 Dec. 1964), pp. 633–638 (cit. on p. 13).

[26]E.C. Gregg and K.David Steidley. “Electrical Counting and Sizing of Mammalian Cells in Suspension”. In: *Biophysical Journal* 5 (4 July 1965) (cit. on pp. 13, 32).

[27]Ralph W. DeBlois, Charles P. Bean, and Roy K.A. Wesley. “Electrokinetic measurements with submicron particles and pores by the resistive pulse technique”. In: *Journal of Colloid And Interface Science* 61 (2 Sept. 1977), pp. 323–335 (cit. on p. 13).

[28]Bjorn de Wagenaar. “Microfluidic single sperm analysis”. PhD. Enschede, The Netherlands: University of Twente, Feb. 2016 (cit. on p. 13).

[29]Tao Sun and Hywel Morgan. “Single-cell microfluidic impedance cytometry: a review”. In: *Microfluidics and Nanofluidics* 8 (4 Apr. 2010) (cit. on p. 13).

[30]Hywel Morgan, Tao Sun, David Holmes, Shady Gawad, and Nicolas G Green. “Single cell dielectric spectroscopy”. In: *Journal of Physics D: Applied Physics* 40.1 (Dec. 2006), pp. 61–70 (cit. on p. 13).

[31] Shady Gawad, Karen Cheung, Urban Seger, Arnaud Bertsch, and Philippe Renaud. “Dielectric spectroscopy in a micromachined flow cytometer: theoretical and practical considerations”. eng. In: *Lab on a Chip* 4.3 (June 2004), pp. 241–251 (cit. on p. 14).

[32] M. Shaker, L. Colella, F. Caselli, P. Bisegna, and P. Renaud. “An impedance-based flow microcytometer for single cell morphology discrimination”. In: *Lab on a Chip* 14 (14 July 2014), pp. 2548–2555 (cit. on pp. 15, 42, 57, 58, 62).

[33] Nicolas Demierre, Thomas Braschler, Pontus Linderholm, et al. “Characterization and optimization of liquid electrodes for lateral dielectrophoresis”. en. In: *Lab Chip* 7.3 (2007), pp. 355–365 (cit. on p. 15).

[34] Xin-She Yang and Slawomir Koziel, eds. *Computational optimization and applications in engineering and industry*. Studies in computational intelligence v. 359. OCLC: ocn733237029. Berlin: Springer, 2011 (cit. on p. 15).

[35] Michael Baudin. *Nelder-Mead User’s Manual*. Apr. 2010 (cit. on p. 16).

[36] Dhananjay Dendukuri, Shelley S. Gu, Daniel C. Pregibon, T. Alan Hatton, and Patrick S. Doyle. “Stop-flow lithography in a microfluidic device”. In: *Lab Chip* 7 (7 2007), pp. 818–828 (cit. on p. 27).

[37] Roberta Stradiotto. *Characterization of electrically active defects at III-N/dielectric interfaces - Defects in GaN/AlGaN MIS–HEMTs*. PhD Thesis. 2016 (cit. on p. 28).

[38] Yongxin Song, Junyan Zhang, and Dongqing Li. “Microfluidic and Nanofluidic Resistive Pulse Sensing: A Review”. en. In: *Micromachines* 8.7 (July 2017), p. 204 (cit. on p. 57).

[39] Yinghua Qiu, Preston Hinkle, Crystal Yang, et al. “Pores with Longitudinal Irregularities Distinguish Objects by Shape”. In: *ACS Nano* 9 (4 Apr. 2015), pp. 4390–4397 (cit. on pp. 57, 58, 63).

[40] Matthew Pevarnik, Ken Healy, Maria Eugenia Toimil-Molares, et al. “Polystyrene particles reveal pore substructure as they translocate”. In: *ACS Nano* 6 (8 Aug. 2012), pp. 7295–7302 (cit. on pp. 57, 63).

[41] Emilie Dressaire and Alban Sauret. “Clogging of microfluidic systems”. In: *Soft Matter* 13 (1 2017), pp. 37–48 (cit. on p. 60).

[42] Yousang Yoon, Seonil Kim, Jusin Lee, et al. “Clogging-free microfluidics for continuous size-based separation of microparticles”. en. In: *Scientific Reports* 6.1 (May 2016), p. 26531 (cit. on p. 60).

[43] Joseph D. Romano and Richard H. Price. “The conical resistor conundrum: A potential solution”. en. In: *American Journal of Physics* 64.9 (Sept. 1996), pp. 1150–1153 (cit. on p. 61).

Additional figures and tables

A

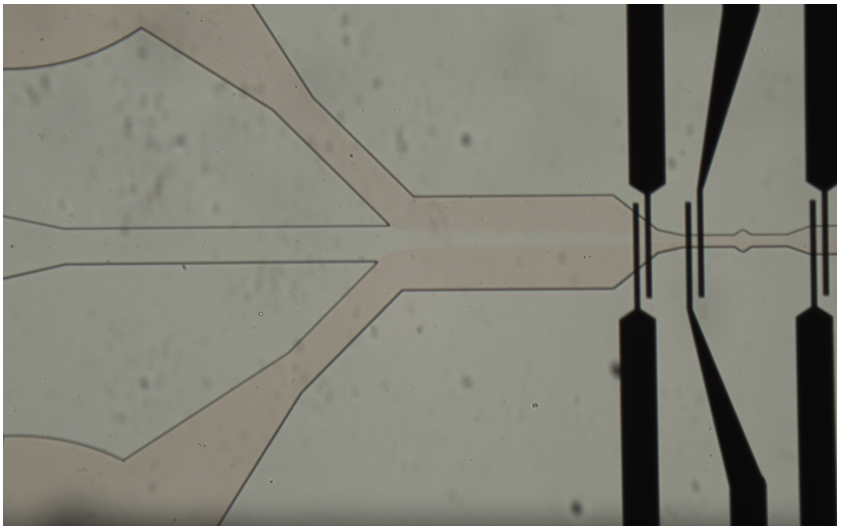

Fig. A.1.: Hydrodynamic flow focusing on the SRIM chip. Sidestreams are coloured with food dye.

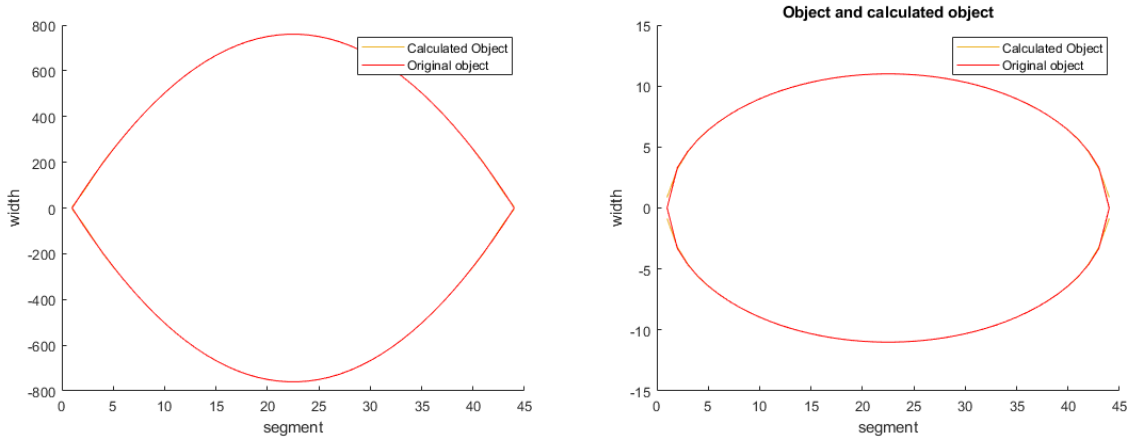

(a) Sphere (3D, cross sectional area)

(b) Sphere (converted from 3D)

Fig. A.2.: Reconstructions made with the Matlab SRIM script from resistance profiles made using the same script. These two images show the conversion from the cross sectional areas to the diameter of the object.

Tab. A.1.: COst function scores for each resistance profile in the classification experiment

Object	Height offset	Front/back offset	Ridge score	Skew score	Sphere score
Teardrop	0	0	4.06E+08	1.05E+07	3.03E+08
Teardrop	0.5	0	4.08E+08	1.09E+07	3.04E+08
Teardrop	1	0	4.18E+08	1.23E+07	3.10E+08
Teardrop	1.5	0	4.18E+08	1.23E+07	3.10E+08
Teardrop	0	-1	3.31E+08	3.59E+06	2.39E+08
Teardrop	0	-3	2.04E+08	1.69E+07	1.32E+08
Teardrop	0	-5	1.10E+08	6.86E+07	5.60E+07
Teardrop	0	-10	4.91E+07	3.74E+08	2.54E+07
Teardrop	0	-15	2.46E+08	9.08E+08	2.31E+08
Teardrop	0	1	4.87E+08	2.59E+07	3.73E+08
Teardrop	0	3	6.69E+08	8.10E+07	5.31E+08
Teardrop	0	5	8.71E+08	1.66E+08	7.07E+08
Teardrop	0	10	1.44E+09	4.85E+08	1.21E+09
Teardrop	0	15	2.07E+09	9.20E+08	1.76E+09
Fused spheroids	0	0	1.71E+07	2.65E+08	2.57E+07
Fused spheroids	0.5	0	1.73E+07	2.65E+08	2.53E+07
Fused spheroids	1	0	1.81E+07	2.65E+08	2.42E+07
Fused spheroids	1.5	0	1.94E+07	2.65E+08	2.24E+07
Fused spheroids	0	-1	2.13E+07	3.33E+08	3.39E+07
Fused spheroids	0	-3	5.48E+07	4.92E+08	7.33E+07
Fused spheroids	0	-5	1.21E+08	6.78E+08	1.42E+08
Fused spheroids	0	-10	4.14E+08	1.24E+09	4.30E+08
Fused spheroids	0	-15	8.44E+08	1.87E+09	8.36E+08
Fused spheroids	0	1	2.13E+07	2.05E+08	2.52E+07
Fused spheroids	0	3	5.49E+07	1.08E+08	4.72E+07
Fused spheroids	0	5	1.21E+08	4.31E+07	9.94E+07
Fused spheroids	0	10	4.14E+08	2.12E+07	3.47E+08
Fused spheroids	0	15	8.44E+08	1.75E+08	7.21E+08
Sphere	0	0	4.55E+07	2.62E+08	9.29E+06
Sphere	0.5	0	4.59E+07	2.62E+08	9.06E+06
Sphere	1	0	4.69E+07	2.63E+08	8.38E+06
Sphere	1.5	0	4.87E+07	2.63E+08	7.29E+06
Sphere	0	-1	4.99E+07	3.31E+08	1.77E+07
Sphere	0	-3	8.47E+07	4.91E+08	5.83E+07
Sphere	0	-5	1.53E+08	6.78E+08	1.29E+08
Sphere	0	-10	4.54E+08	1.24E+09	4.24E+08
Sphere	0	-15	8.97E+08	1.88E+09	8.42E+08
Sphere	0	1	4.99E+07	2.02E+08	8.94E+06
Sphere	0	3	8.48E+07	1.06E+08	3.22E+07
Sphere	0	5	1.53E+08	4.41E+07	8.64E+07
Sphere	0	10	4.54E+08	3.22E+07	3.42E+08
Sphere	0	15	8.97E+08	2.00E+08	7.28E+08

Appendix: Code

B

B.1 SRIM code

```
%%% Shing Long Lin 21-10-2020
close all;%clear all;
%% parameters

%extra length added to the calculated object, to be determined to be zero, representing uncertainty
%in length
unknownlength=0;

%scaling factor for the area of the channel
channel_scale=1;

%noise in R, uniformly distributed!
percent_noise=0;% 0.001 is challenging yet solvable for the full length sperm
rng('default');%fixes the random number generator seed for reproducible results. Look out for overoptimizing for this seed!

%lower and upper bounds for object width for optimizer
Optimizerlowerbound=0;
Optimizerupperbound=2000;

%deviation in real channel size versus known size
Channel_uncertainty=0.0;
absolute_uncertainty=0;%3indexes=1um deviation, not realistic as normally whole blocks should be around the same value

%amount of steps to start away from begin of channel and end from end of channel
Reduced_path=0;

%% 22 Sphere
i=linspace(-22,22,44);
sphere=pi*(22^2-i.^2);
%Object=sphere;

%% 22 skew 3D
i=linspace(-22,22,44);
ellipse=sqrt((22^2-i.^2));
skewx=linspace(0.2,1.4,44);
skewed_ellipse=2*skewx.*ellipse+4;
skew=pi*(0.5*skewed_ellipse).^2;
Object=skew;

%% Fused_22_22 3D
```

```
i=linspace(-11,11,22);
fCircle25=2*sqrt(22^2-(i*2).^2);
Fused_22_22=horzcat(fCircle25(1:17),fCircle25(7:22));
fused=pi*(.5*Fused_22_22).^2;
%Object=fused;
%% Tapered Channel parameters

L_chan=80;
W_chan=50;
V_in=0.05;
H_chan=50;
L_extra=100;
slope=1;
%every slice is going to be 10^-6 thick

Channel=zeros(1,(L_chan+L_extra));
Channel(1:L_extra/2)=W_chan;
Channel((L_extra/2+L_chan):L_chan+L_extra)=W_chan;
%% Straight tapered channel
Channel((L_extra/2):(L_extra/2+L_chan/2))=W_chan+linspace(0,(slope*L_chan/2),(L_chan/2+1));
Channel((L_extra/2+L_chan/2):(L_extra/2+L_chan))=W_chan+linspace((slope*L_chan/2),0,(L_chan
    /2+1));

%% Object extra whitespace
Object=horzcat(zeros(1,28),Object,zeros(1,28));

%% Channel initialization
if ((length(Object)+unknownlength)>(length(Channel)-1))
    error('Object too long');
end
Channel=Channel.*channel_scale;
zerofill_unknown=zeros(1,length(Channel)-length(Object)-unknownlength);
%extra zeroes for concatenation to x for subtraction
Objectfilled=horzcat(Object,zeros(1,length(Channel)-length(Object)));
%all extra zeroes concatenated to object for calculation of R

%add uncertainty to channel
clb = 1-Channel_uncertainty;
cub = 1+Channel_uncertainty;
channeldeviation = (cub-clb).*rand(size(Channel)) + clb;
%noise is random between lb (lower bound) and ub(upperbound=1)
newChannel=channeldeviation.*Channel+rand(size(Channel)).*absolute_uncertainty;

Channelarea=Channel*50;
Channel=Channelarea;

%% Calculation of resistance per object shift

A_inv=zeros(length(Channel)-length(Object)-unknownlength,length(Channel));
A_inv_corr=zeros(length(Channel)-length(Object)-unknownlength,length(Channel));
R=zeros(length(Channel)-length(Object)-unknownlength-2*Reduced_path,1);
R_corr=zeros(length(Channel)-length(Object)-unknownlength-2*Reduced_path,1);
for n=0:(length(Channel)-length(Object)-unknownlength-2*Reduced_path)
    %Shifts the channel negatively to simulate moving the object, produces the resistance
        contribution of each index horizontally, each shift vertically
```

```
    A_inv(n+1,:)=(circshift(Channel,-(n+Reduced_path))-Objectfilled).^-1;
    A_inv_corr(n+1,:)=((circshift(Channel,-(n+Reduced_path))-Objectfilled)*10^-12).^-1;
    R(n+1)=sum(A_inv(n+1,:));
    R_corr(n+1)=10^-6*sum(A_inv_corr(n+1,:));
end

Current=0.05./R_corr;
%% add noise to Resistance
lb = (100-percent_noise)/100;
ub = (100+percent_noise)/100;
noiselevel = (ub-lb).*rand(size(R)) + lb;
%noise is random between lb (lower bound) and ub(upperbound=1)
NoiseR=noiselevel.*R;
R_orig=R;
R=NoiseR;

R_empty=sum(Channel.^-1);
R_empty_corr=R_empty*10^6*10^-6/(10^-6);%correction for width, length and height
R_empty_comsol=36353.854*(50*10^-6);

%%% Calculation of object from model
%%function g is made as an array of function, which becomes a cell, R_sim evaluates the function with
%%Object for checking ii is used for shifting the x functions f is the objective function, minimizing
%%the difference between the measured R and the evaluation of the x function
% ii=0:(length(Channel)-length(Object)-unknownlength-2*Reduced_path);
% g = @(x) arrayfun(@(n) sum((circshift(Channel,-(n+Reduced_path))-horzcat(x,zerofill_unknown)).^-1), ii, 'UniformOutput',false);
% reg_scale=10^-6;
% h = @(x) reg_scale*sum((x(1:end-1)-x(2:end)).^2);
% R_sim=cell2mat(g(horzcat(Object,zeros(1,unknownlength)))');
% scaling=10^6;
%%f=@(x)scaling*sum(sqrt((R-cell2mat(g(x)')).^2));
%%f=@(x)scaling*sum(((R-cell2mat(g(x)')).^2));
% f=@(x)scaling*sqrt(sum((R-cell2mat(g(x)')).^2))+h(x);
%
% options=optimoptions(@fmincon,'Display','iter','OptimalityTolerance',10^-6,'MaxFunctionEvaluations',30000,'MaxIterations',3000);
% x=fmincon(f,ones(1,length(Object)+unknownlength),[],[],[],[],ones(1,length(Object)+unknownlength)*Optimizerlowerbound,ones(1,length(Object)+unknownlength)*Optimizerupperbound,[],options);%bounded with 0 as lower bound
%%the first field is the objective function, the second field is the amount of dimensions (thus the
%%possible length) of the object, then come several constraint functions which are skipped. Next are
%%the upper bound and lower bound vectors whic hrestrict the solution space to positive numbers below
%%the width of the channel or some other maximum value Optimizerupperbound

%% Calculation of object from comsol
%%function g is made as an array of function, which becomes a cell, R_sim evaluates the function with
%%Object for checking ii is used for shifting the x functions f is the objective function, minimizing
```

```
%%the difference between the measured R and the evaluation of the x function
%%Object=zeros(44,1);%Dummy object for length estimation
% correction_factor=1.00;
% ii=0:(length(Channel)-length(Object)-unknownlength-2*Reduced_path);
% g = @(x) arrayfun(@(n) correction_factor*sum((circshift(Channel,-(n+Reduced_path))-horzcat(x,zerofill_unknown)).^-1*10^6), ii, 'UniformOutput',false);
% R_sim=cell2mat(g(horzcat(Object,zeros(1,unknownlength)))');
% scaling=10^0;
% f=@(x)scaling*sum((R_sphere-cell2mat(g(x)')+flat_corr).^2);
%
% options=optimoptions(@fmincon,'Display','iter','OptimalityTolerance',10^-6,'MaxFunctionEvaluations',30000,'MaxIterations',3000);
% x=fmincon(f,600*ones(1,length(Object)+unknownlength),[],[],[],[],ones(1,length(Object)+unknownlength)*Optimizerlowerbound,ones(1,length(Object)+unknownlength)*Optimizerupperbound,[],options);%bounded with 0 as lower bound
%%the first field is the objective function, the second field is the amount of dimensions (thus the
%%possible length) of the object, then come several constraint functions which are skipped. Next are
%%the upper bound and lower bound vectors whic hrestrict the solution space to positive numbers below
%%the width of the channel or some other maximum value Optimizerupperbound

%%% Calculation of object from comsol with regularisation
%function g is made as an array of function, which becomes a cell, R_sim evaluates the function with
%Object for checking ii is used for shifting the x functions f is the objective function, minimizing
%the difference between the measured R and the evaluation of the x function
%Object=zeros(44,1);%Dummy object for length estimation
correction_factor=1;
ii=0:(length(Channel)-length(Object)-unknownlength-2*Reduced_path);
g = @(x) arrayfun(@(n) correction_factor*sum((circshift(Channel,-(n+Reduced_path))-horzcat(x,zerofill_unknown)).^-1*10^6), ii, 'UniformOutput',false);
reg_scale=0;
h = @(x) reg_scale*sum((x(1:end-1)-x(2:end)).^2);
reg_scale2=10^3;
k =@(x) reg_scale2*sum(x(1:10)+x(end-9:end));
R_sim=cell2mat(g(horzcat(Object,zeros(1,unknownlength)))');
scaling=10^0;
corr_constant=-5000;
f=@(x)scaling*sum((-R_ridge(21:end-20)-cell2mat(g(x)')+corr_constant).^2)+h(x);

options=optimoptions(@fmincon,'Display','iter','OptimalityTolerance',10^-6,'MaxFunctionEvaluations',30000,'MaxIterations',3000);
x=fmincon(f,ones(1,length(Object)+unknownlength),[],[],[],[],ones(1,length(Object)+unknownlength)*Optimizerlowerbound,ones(1,length(Object)+unknownlength)*Optimizerupperbound,[],options);%bounded with 0 as lower bound
%the first field is the objective function, the second field is the amount of dimensions (thus the
%possible length) of the object, then come several constraint functions which are skipped. Next are
%the upper bound and lower bound vectors whic hrestrict the solution space to positive numbers below
%the width of the channel or some other maximum value Optimizerupperbound
```

```
177
178 %% Plotting of object and channel and evaluation of found object
179 % RMS=Evaluate_Object_from_channel(x, Object);
180 % %figure; hold on;plot(Object);plot(x);
181 % plot_double2(Object,x);legend('Calculated Object','Original object');xlabel("segment");
      ylabel("width");text(length(x)-20,-max(x)+2,sprintf('RMS = %5.4f', RMS))
182 % %figure;hold on;plot(Channel);plot(x);plot(Object);
183 % plot_double3(Object,x,Channel);legend('Channel','Calculated Object', 'Original Object');
      xlabel("x-axis segment");ylabel("width");text(length(Channel)-35,-1800,sprintf('RMS =
      %5.4f', RMS));%title('Object, reconstructed object and channel');
184
185 %% Plotting of 3D object and channel and evaluation of found object
186 RMS=Evaluate_Object_from_channel(x, Object);
187 %figure; hold on;plot(Object);plot(x);
188 plot_double2(2*(Object/pi).^.5,2*(x/pi).^.5);legend('Reconstructed object','Original object
      ');xlabel("segment (\mum)");ylabel("diameter(\mum)");text(.8*length(x),-((max(x)/pi)
      .^.5)-3,sprintf('RMS = %5.1f', RMS));%title('Object and calculated object')
189 %figure;hold on;plot(Channel);plot(x);plot(Object);
190 %plot_double3(2*(Object/pi).^.5,2*(x/pi).^.5,Channel/50);legend('Channel','Calculated
      Object', 'Original Object');xlabel("x-axis segment");ylabel("width");text(length(
      Channel)-47,-35,sprintf('RMS = %5.4f', RMS));%title('Object, reconstructed object and
      channel');title('2D view of 3D sphere');
191
192 %{
193
194 dim1=linspace(0,5,201);
195 dim2=linspace(0,5,201);
196 dim3=zeros(201,201);
197
198 for n=1:length(dim2)
199     for j=1:length(dim1)
200         dim3(j,n)=f([dim1(n),dim2(j)]);
201     end
202 end
203 logdim3=log10(dim3);
204 figure;surf(dim1,dim2,logdim3,'Edgecolor','none');view(2);colorbar();title(sprintf('10log(
      Error), noise = %.0f%%',percent_noise));xlabel('Object[1]');ylabel('Object[2]');text
      (0.3,0.3,sprintf('RMS = %5.4f', RMS));
205 %logdim3(41,161)=-3;
206 %[pdim1,pdim2] = gradient(logdim3);
207 %figure;contour(dim1,dim2,logdim3);hold on;quiver(dim1,dim2,pdim1,pdim2);
208 %figure;surf(dim1,dim2,(pdim1.^2+pdim2.^2).^0.5,'Edgecolor','none');view(2);colorbar();
      xlabel('Object[1]');ylabel('Object[2]');title('Gradient of cost function');
209 %}
210 function plot_double2(object,x)
211    figure;hold on;plot(.5*x,'color',[0.9290 0.6940 0.1250]);plot(.5*object,'r');plot(-.5*x,
         'color',[0.9290 0.6940 0.1250]),plot(-.5*object,'r');
212 end
213 function plot_double3(object,x,channel)
214    figure;plot(.5*channel,'b');hold on;plot(.5*x,'color',[0.9290 0.6940 0.1250]);plot(.5*
         object,'r');plot(-.5*x,'color',[0.9290 0.6940 0.1250]),plot(-.5*object,'r');plot
         (-.5*channel,'b');
215 end
```

B.2 Zurich data to Matlab

```
V.in=2;
%Data=[cast(stream004_00009.demods(1).sample.timestamp,'double'); stream004_00009.demods(1).sample.x-stream004_00009.demods(2).sample.x; stream004_00009.demods(1).sample.y-stream004_00009.demods(2).sample.y]';
%Data=[cast(stream004_00009.demods(1).sample.timestamp,'double'); stream004_00009.demods(1).sample.x; stream004_00009.demods(1).sample.y]';
%Data=[cast(stream000_00020.demods(1).sample.timestamp,'double'); stream000_00020.demods(1).sample.x; stream000_00020.demods(1).sample.y]';
%Data=table2array(dev1569demods1sample00000);
%Datamod1=table2array(dev1569demods1sample00000);
%Data(:,2:3)=Data(:,2:3)-Datamod1(:,2:3);
%close all;
    %% Extract the colums and process to usable units with V_in.
%Data = table2array(Data_orig_stream002(:, [1,2,3])); %Extract from structure
Data=readtable('dev1569_demods_0_sample_00000.csv');
Data=table2array(Data);
Data=Data(:,[2 3 4]);
TimeStamp = Data(1:end-100,1)-Data(1,1); %all rows of the first column for time data.
%SampleRate = TimeStamp(2,1);
SampleRate = 14400;
T.data = zeros(length(TimeStamp),1);
for i=1:length(TimeStamp)-1
    T.data(i+1,1) = 1/SampleRate*i;
end
X = Data(1:end-100,2);    %all rows of the second column for the real part
Y = Data(1:end-100,3);    %all rows of the third column for the imaginary part
%Find V (vrms) from the real and imaginary part.
V.data = (X.^2+Y.^2).^0.5/1000; %Vrms = (X^2+Y^2)^0.5
Phase.data = atan2(Y,X)*180/pi; %Phase = atan2(Y,X)
%Convert to impedance:
Z.data = V.in/(2)^0.5./V.data; %Gives |Z|
figure;plot(T.data,Z.data);xlabel('time(s)');ylabel('|Z|(\Omega)');
```

B.3 Time to position translation Zurich data

```
close all;
flow_speed=0.5*10^-6;

Peak1=Z.data(find(T.data>=1.08749&T.data<=1.130524+0.00));
Peak1orig=Peak1;
middle=(length(Peak1)+1)/2;
speed=zeros(1,length(Peak1));
width=zeros(1,length(Peak1));
position=zeros(1,length(Peak1));
timestep=1/230269;
position(middle)=0;
for i=0:(length(Peak1)-1)/2
    if abs(position(middle+i))>(40*10^-6)
        width(middle+i)=50*10^-6;
    else
        width(middle+i)=50*10^-6+((40-abs(position(middle+i)*10^6))/40)*40*10^-6;
```

```
    end
    speed(middle+i)=flow_speed/1000/60/(width(middle+i))/(50*10^-6);
    position(middle+i+1)=position(middle+i)+speed(middle+i)*timestep;
end
for j=0:(length(Peak1)-1)/2
    if abs(position(middle-j))>(40*10^-6)
        width(middle-j)=50*10^-6;
    else
        width(middle-j)=50*10^-6+((40-abs(position(middle-j)*10^6))/40)*40*10^-6;
    end
    speed(middle-j)=flow_speed/1000/60/(width(middle-j))/(50*10^-6);
    if(j<(length(Peak1)-1)/2)
        position(middle-1-j)=position(middle-j)-speed(middle-j)*timestep;
    end
end

figure;plot(width);
figure;plot(speed);
figure;plot(position);

position_discrete=round(position*10^6)/10^6;
figure;plot(position_discrete);

gaps=position_discrete(2:end)-position_discrete(1:end-1);

for i=1:length(gaps)
    j=length(gaps)-i+1;
    if gaps(j)>1.5*10^-6 && j>1
        Peak1=[Peak1(1:j-1); (Peak1(j-1)+Peak1(j))/2; Peak1(j:end)];
    elseif gaps(j)>1.5*10^-6 && j==1
           Peak1=[Peak1(j); Peak1(j:end)];
    end
end

figure;plot(Peak1);hold on;plot(Peak1orig);
figure;plot(position(1:end-1),Peak1);xlabel('position (\mum)');ylabel('Impedance|Z|');

[unpos,~,unposind]=unique(position_discrete(2:end));
SRIMPeak1=accumarray(unposind,Peak1,[],@mean);
```

Appendix: Protocols

C

C.1 Chip casting and curing

Requires:

- 30 mL PDMS
- 3 mL PDMS curing agent
- 50 mL tube
- master wafer
- scotch tape
- cutting tool

1. Put scotch tape around wafer to form a sidewall. Make bottom leak proof with additional scotch tape. Due to tension in the tape, the sidewall may taper inwards a bit. Dust off the wafer with compressed air and put the wafer back in its container with the lid on.
2. In a 50mL tube, weigh approximately 30 mL PDMS and 3 mL curing agent in a 10:1 ratio and mix well for 1 minute. The mixture should appear bubbly after mixing.
3. Cast the PDMS onto the wafer
4. Degas the PDMS in the vacuum chamber. Pulse the vacuum chamber twice by returning pressure to atmosphere and applying vacuum again afterwards. This helps to speed up the degassing process. Leave the wafer under the vacuum for at least 30 minutes until the bubbles in the PDMS are gone.
5. Bake the PDMS at 60° C for at least 60 minutes. You can check for hardness by lightly pressing a glove covered finger on an unused corner. The glove should not leave a mark. The PDMS can also be left in the oven overnight.
6. Take the PDMS out of the oven when done. Cool for several minutes. Remove all the scotch tape. Lightly peel the PDMS from the edges of the wafer.
7. Cover the top side of the PDMS with rows of scotch tape to protect the PDMS from dust and dirt. Run the tape diagonally relative to any cutting lines to improve visibility of the cutting lines later on.

8. When the edges are loose and the top side of the PDMS is covered in tape, peel the PDMS off the wafer in a direction parallel to the channels or other features. Immediately cover this side in scotch tape too to protect against dust and dirt. Take note of the direction once again.
9. Cut the PDMS along the cutting lines.

C.2 Chip alignment and bonding

1. Set plasma over to standby according to oven instructions.
2. Punch reservoirs using the circular punches. Recommended reservoir sizes are 0.7 mm for the needle hole and 3 mm for the droplet reservoir.
3. Remove scotch tape from both sides and place chip with feature side upwards and the glass slide with the electrodes in the plasma oven.
4. Decrease the pressure to 60mTorr, then open the valve for atmospheric oxygen and activate the plasma for 45 seconds, as per the oven instructions.
5. Remove both parts of the chip from the plasma oven and cover to prevent dust contamination. Let the surfaces deactivate for 15 minutes to prevent overstrengthening of the bonding.
6. Place the PDMS chip with its features facing downwards in the chip carrier of the alignment tool and use it to align the PDMS chip with the needles of the alignment tool. The needles should be above the corner supports of the chip carrier.
7. Lower the needles into the PDMS. After the needles have pierced the PDMS about halfway through, raise the needles to lift the PDMS off the carrier.
8. Place the PCB containing the glass slide in the alignment tool. Be careful not to touch the bottom side of the PDMS.
9. Use the microscope to align the channels in the PDMS with the electrodes on the glass slide, while lowering the PDMS onto the glass slide.
10. When the PDMS chip is fully lowered onto the glass slide, use the small bottle that comes with the alignment tool to keep the chip assembly in place while raising the needles.
11. Lightly press the PDMS with a glove covered finger to ensure good contact. Be careful not to press too hard and squeeze the channels shut.

12. Cover the PDMS with scotch, label the scotch and place the assembly in the oven for 30 minutes at 60° C to promote the forming of chemical bonds.

C.3 Chip connection for experiments

1. Clean the syringe and the tubing by rinsing with deionized water. Attach the syringe to the syringe pump.
2. Place the chip assembly on the microscope table and connect the electrical connections and the tubing.
3. Add 10 μL diluted food coloring dye to the chip reservoir. Run the syringe pump at -1 μL/min. Check the microscope feed for leakage in the chip.
4. If no leakage is detected, remove the dye from the reservoir and add 10 μL electrolyte solution to the reservoir. The solution will slowly replace the dye in the channel. Wait for the impedance to stabilize.
5. Check if the impedance is as expected. Deviations might suggest short circuits due to leakage or faulty PCB connections.
6. If the impedance values appear correct, empty the reservoir and add 15 μL PLL-PEG. Let the channel fill with PEG and then decrease the flow to -0.2 μL/min. Allow the channel to be incubated for 15 minutes.
7. Rinse the chip with deionised water by emptying the reservoir and adding 10 μL water and running it through the chip with -1μL/min for several minutes. The chip is now ready for use.

C.4 SU-8 master wafer

Materials

- 3 inch silicon wafer
- HNO3(99%)
- Negative resist: SU-8 50 for 50 um height chips
- Negative resist: SU-8 5 for 8 um particles

- RER600 (ARCH Chemicals)
- Mask with channels

Process Flow

Step	Process				User comments
1		5 min in 99% HNO3 (beaker 1)			
2	Standard cleaning	5 min in 99% HNO3 (beaker 2)			
3	Wetbench 16	Quick dump rinse (QDR), until DI resistivity >10 Ωm			
4		10 s HF dip			
5		QDR			
6		Single wafer spin drying (2500 rpm, 60 c)			
7	Photolithography Wetbench 24	10 min dehydration bake @ 120°C			Let cool down to RT
		Spin SU-8 Ramp of 100 rpm/s to 500 rpm, 10 s. Ramp of 300 rpm/s to:			
11		SU8-5 8 um 1800 rpm, 30 s	SU8-5 10 um 1400 rpm, 30 s	SU8-50 50 um 3250 rpm, 30 s	
12		Prebake Start @ 25°C 1 min bake @ 50°C 1 min bake @ 65°C 3 min bake @ 95°C Ramp down to 25°C (5°C/2 min)	Prebake Start @ 25°C 1 min bake @ 50°C 1 min bake @ 65°C 3 min bake @ 95°C Ramp down to 25°C (5°C/2 min)	Prebake Start @ 25°C 10 min bake @ 50°C 10 min bake @ 65°C 320 min bake @ 95°C Ramp down to 25°C (5°C/2 min)	
13	EVG620 Mask aligner	Exposure, HG-lamp (12 mW/cm2, 10 s) Top side, soft contact, separation 50 μm	Exposure, HG-lamp (12 mW/cm2, 10 s) Top side, soft contact, separation 50 μm	Exposure, HG-lamp (12 mW/cm2, 22.5 s) Top side, soft contact, separation 50 μm	
14	Wetbench 24	Post exposure bake Start @ 25°C 1 min bake @ 50°C 1 min bake @ 65°C 2 min bake @ 80°C Ramp down to 25°C (5°C/2 min)	Post exposure bake Start @ 25°C 1 min bake @ 50°C 1 min bake @ 65°C 2 min bake @ 80°C Ramp down to 25°C (5°C/2 min)	Post exposure bake Start @ 25°C 5 min bake @ 50°C 5 min bake @ 65°C 10 min bake @ 80°C Ramp down to 25°C (5°C/2 min)	
16		Developer: RER600			
17	Development	Spray gun, 10 cycles of 30 seconds			
18	Wetbench 24	Rinse the wafer manually with RER600			
19		Rinse with IPA to remove remains of RER600			
20		Spin dry, 2500 rpm, 60 s			
21		Check the result and perform extra cycles if necessary.			

22	Hardbake	Hardbake Start @ 25°C 1 min bake @ 50°C 1 min bake @ 65°C 1 min bake @ 95°C 10 min bake @ 120°C Ramp down to 25°C (5°C/2 min)	
23	Height determination Dektak	Determine the height of the channels with the Dektak (Stylus radius: 2.5 μm)	

C.5 SU-8 Custom microparticles

Materials

- 4 inch silicon wafer
- HNO3(99%)
- HF (1%)
- Hexamethyldisilazane (HMDS)
- Positive resist: Olin OiR 906-17
- Negative resist: SU-8 25 for 30 um particles
- Negative resist: SU-8 5 for 8 um particles
- RER600
- Mask with objects (non-mirror, IW)

Process flow

Step	Process		User comments
1		5 min in 99% HNO3 (beaker 1)	
2	Standard cleaning	5 min in 99% HNO3 (beaker 2)	
3	Wetbench 16	Quick dump rinse (QDR), until DI resistivity >10 Ωm	
4		10 s HF dip	
5		QDR	
6		Single wafer spin drying (2500 rpm, 60 c)	

7	Photolithography	10 min dehydration bake @ 120°C		Let cool down to RT
8	Wetbench 21	Spin HMDS (4000 rpm, 30 s)		
9		Spin Olin Oir 907-17 (4000 rpm, 30 s)		
10		10 min prebake @ 150°C		Let cool down to RT
11	Wetbench 24	8 um particles: Spin SU-8 5 Ramp of 100 rpm/s to 500 rpm for 10 s. Ramp of 300 rpm/s to 2500 rpm for 30 s	30 um particles: Spin SU-8 25 Ramp of 100 rpm/s to 500 rpm for 10 s. Ramp of 300 rpm/s to 2000 rpm for 30 s	
12		Prebake Start @ 25°C 1 min bake @ 50°C 1 min bake @ 65°C 3 min bake @ 95°C Ramp down to 25°C (5°C/2 min)	Prebake Start @ 25°C 10 min bake @ 50°C 10 min bake @ 65°C 45 min bake @ 95°C Ramp down to 25°C (5°C/2 min)	
13	EVG620 Mask aligner	Exposure, HG-lamp (12 mW/cm2, 10 s) Top side, soft contact, separation 50 μm	Exposure, HG-lamp (12 mW/cm2, 24 s) Top side, soft contact, separation 50 μm	
14	Wetbench 24	Post exposure bake Start @ 25°C 1 min bake @ 50°C 1 min bake @ 65°C 2 min bake @ 80°C Ramp down to 25°C (5°C/2 min)	Post exposure bake Start @ 25°C 5 min bake @ 50°C 5 min bake @ 65°C 10 min bake @ 80°C Ramp down to 25°C (5°C/2 min)	
15		Wrap in aluminum foil		
16	Development	Transfer wafer into beaker with RER600 Cover with aluminum foil		
17	Chemical lab BIOS	30 min ultrasonic bath at max power		Check wafer, if particles still stuck, repeat.
18		Remove wafer from beaker and rinse above beaker with RER600, then with IPA		
19		Dry wafer		
20	Resuspend	Transfer solution into 50 mL tubes.		
21		Centrifuge		
22		Remove solution and resuspend particles in IPA		Repeat step 21&22 three times
23		Centrifuge		
24		Remove solution and resuspend particles in DI-water		Repeat step 23&24 three times
25	Usage	Before use, centrifuge, remove solution and resuspend in appropriate medium		
26		If particles clump, add 0.1% v/v Tween 20 to particle solution.		

Colophon

This thesis was typeset with LaTeX 2_ε. It uses the *Clean Thesis* style developed by Ricardo Langner. The design of the *Clean Thesis* style is inspired by user guide documents from Apple Inc.

Download the *Clean Thesis* style at `http://cleanthesis.der-ric.de/`.